Marine Structures 72 (2020) 102781

Contents lists available at ScienceDirect

Marine Structures

journal homepage: http://www.elsevier.com/locate/marstruc

Design, modelling, and analysis of a large floating dock for spar floating wind turbine installation

Zhiyu Jiang [a,*], Rune Yttervik [b], Zhen Gao [c,d,e], Peter Christian Sandvik [f]

[a] Department of Engineering Sciences, University of Agder, N-4898 Grimstad, Norway
[b] Research and Development, Equinor ASA, Trondheim, Norway
[c] Centre for Research-based Innovation of Marine Operations (SFI MOVE), Norwegian University of Science and Technology (NTNU), N-7491, Trondheim, Norway
[d] Department of Marine Technology, NTNU, Trondheim, Norway
[e] Centre for Autonomous Marine Operations and Systems (SFF AMOS), NTNU, Trondheim, Norway
[f] SINTEF Ocean AS, Trondheim, Norway

ARTICLE INFO

Keywords:
Offshore installation
Spar floating wind turbine
Floating dock
Design optimisation
Hydrodynamics
Numerical modelling
Time domain
Frequency domain
Dynamic response

ABSTRACT

Installation of floating wind turbines at the offshore site is a challenging task. A significant part of the time efficiency and costs are related to the installation methods which are sensitive to weather conditions. This study investigates a large floating dock concept, which can be used to shield a floating wind turbine during installation of tower, nacelle, and rotor onto a spar foundation. In this paper, the concept is described in detail, and a design optimisation is carried out using simple design constraints. Hydrodynamic analysis and dynamic response analysis of the coupled system of the optimum dock and spar are conducted. Two spars of different sizes are considered, and the motion responses of the spars with and without the dock in irregular waves are compared. Through analysis of the motion spectra and response statistics, dynamic characteristics of the coupled system is revealed. The present design of the dock reduces the platform-pitch responses of the spars and potentially facilitates blade mating, but may deteriorate the heave velocity of the spars in swell conditions. Finally, future design aspects of the floating dock are discussed.

1. Introduction

Globally, wind energy is one of the most attractive forms of renewable energy resources, and the annual energy production of wind energy grows at a rate of 25–30% [1]. Since 1990s, offshore wind farms are increasingly popular. To date, more than 81 offshore wind farms across 10 European countries have been constructed. The average water depth of those offshore wind farms is close to 30 m (m), and monopile foundation is the dominant type of support structures [2].

Partly due to geographical limitations, countries are assessing deep-water offshore sites for future development of wind energy facilities. As water depth increases, wind turbines supported by floating foundations like spars or semi-submersibles can be cost-effective solutions. The Hywind pilot park, the world's first floating wind farm, has been delivering power to 22,000 households in the UK since October 2017 [3]. Although proven technologies from the oil and gas industry are readily applicable, commercial deployment of floating wind technology is still at a small scale.

Since 2000s, extensive activities have been observed within the research and development of offshore wind technologies. For

* Corresponding author. (Zhiyu Jiang).
E-mail addresses: zhiyu.jiang@uia.no (Z. Jiang), ruy@equinor.com (R. Yttervik), zhen.gao@ntnu.no (Z. Gao), pcsandvik@gmail.com (P.C. Sandvik).

https://doi.org/10.1016/j.marstruc.2020.102781
Received 14 May 2019; Received in revised form 20 March 2020; Accepted 20 April 2020
Available online 28 May 2020

example, advanced numerical simulation tools including FAST [4] and HAWC2 [5] make possible coupled aero-hydro-servo-elastic analysis of offshore wind turbines (OWTs) in various loading conditions. Today, the levelised cost of energy of the bottom-fixed offshore wind technology has been brought to a competitive level. Still, the costs related to assembly and installation can account for 6.3% of the capital expenditure for an fixed-bottom offshore wind reference project according to Moné et al. [6]. For installations of fixed-bottom offshore wind turbines, traditional methods are crane operations using jacke-up or floating installation vessels. Among a few research works that focus on installation of foundations of OWTs, Sarkar et al. [7] demonstrated an installation concept using a floating vessel along with a floatable subsea structure for installing monopile-type OWTs. Guachamin-Acero et al. [8] developed an installation concept for small crane vessels using the inverted pendulum principle in which the pre-assembled rotor, nacelle and tower can be installed via rotation through a rotating frame at the tower base. Esteban et al. [9] reviewed the methods used in the offshore installation of gravity-based structures in offshore wind facilities operating in Europe. Regarding the installation of wind turbine blades, researchers started to address the technical challenges and risks that exist during the mating phase in recent years. For example, Ren et al. [10] proposed an active tugger control method to facilitate the single-blade installation. Verma et al. [11] identified failure modes of blade roots during an offshore mating task and provided guidelines to aid onboard decision making.

Compared with bottom-fixed OWTs, floating wind turbines (FWTs) face even greater challenges in offshore installations, and the installation methods are strongly concept-dependent. The spar, semisubmersible and tension leg platform are three main types of support structures for FWTs, which have quite different philosophies for installation because of their differences in towability, platform stability, and mooring and anchor systems [12]. Hywind is a well-known example of FWTs suitable for operation in deep waters and harsh environments typical of the North Sea. To lower the risks associated with offshore installations, upending of the spar foundation and assembly of wind turbine components were performed at a well-sheltered location in Norway. Then, the unit was towed to the operation site and hooked up to the mooring system [13]. Such an installation procedure is less feasible for wind farms far from coastlines which provide deep sheltered areas. Generally, low sea states are required for offshore installations that take place in open seas [14], and frequency composition of the sea state is important. Sea states with significant energy in low frequencies are problematic for certain tasks like mating because of motions of the pre-assembled floating units and the crane vessels involved.

To elevate the competitiveness of floating wind technology, alternative installation methods to expand the weather window and avoid unexpected delays are desired. In 2014, a few novel concepts were proposed by industrial participants in the Hywind installation challenge [15], and some concepts promoted the use of specialised equipment for wind turbine installation. Recently, Hatledal et al. [16] and Jiang et al. [17] presented numerical investigations on a catamaran installation vessel for installation of preassembled rotor-nacelle-tower assemblies onto spar foundations. This installation concept involves a catamaran with a dynamic positioning system, lifting grippers, and sliding grippers. The catamaran is designed to perform offshore installations in open seas, where the spar foundation experiences motions that should be compensated during the mating process of wind turbine assemblies [18].

To further address the installation challenges of the floating wind technology in open seas, we study a large floating dock concept in this paper. The focus is on the installation platform, not the FWTs. In the following, Sec. 2 presents the main idea of the concept and discusses the assumptions and considerations for the design. An optimum dock is also presented in this section. Sec. 3 presents the hydrodynamic analysis by the panel method; Sec. 4 introduces preliminary design of the mooring system for the dock; Sec. 5 describes the two spars selected for this study; Sec. 6 presents the main results from the coupled dynamic simulations, and Sec. 7 draws the conclusion. The aim of this work is to present the floating dock concept, to identify the dynamic characteristics of the dock-spar systems in operational conditions and to assess the potential of this concept for offshore mating tasks.

2. The large floating dock concept

2.1. General

By industrial practices, offshore installation of a spar FWT requires a heavy-lift vessel with cranes, and the spar foundation can either be mated with a pre-assembled rotor-nacelle-tower assembly or with individual tower, nacelle, and blades, depending on the installation method chosen [19]. Regardless of the method, both the spar FWTs and installation vessels are floating structures. For a spar foundation exposed to open seas, a particular challenge arises when the upended spar foundation needs to be mated with other components. The wave loads may induce heave and pitch motions of the spar foundation. The heave motion could create impact loads during mating of the wind turbine tower assembly [18], and the pitch motion causes horizontal motions at the tower top. This is challenging to the alignment and mating processes of wind turbine blades [20].

The proposed large floating dock is intended to provide a shelter for the spar foundation in open seas and to facilitate the installation process. Fig. 1 schematises the basic construct of the concept. The dock has a cylindrical shape with an internal moonpool and includes storage space for components, an accommodation unit, lifting cranes on the upper deck, ballast compartments within the internal and external walls, bilge tanks, and a gate. The simple geometry of the dock is proposed primarily for the convenience of manufacturing. The bilge tanks can be used to store fixed ballast and will bring additional viscous damping to the dock during operation. A mooring system is used for station-keeping of the floating dock, and mooring lines with winches should be permanently installed on the dock. A description of the design variables can be found in Sec. 2.5.

2.2. Transit and operation of the floating dock

After being produced from a shipyard, the dock has a permanent hull form but can change its draft during transit and operation. This is achieved by adjusting the distributed ballast system. During transit, the dock should have a small draft to pass shallow waters.

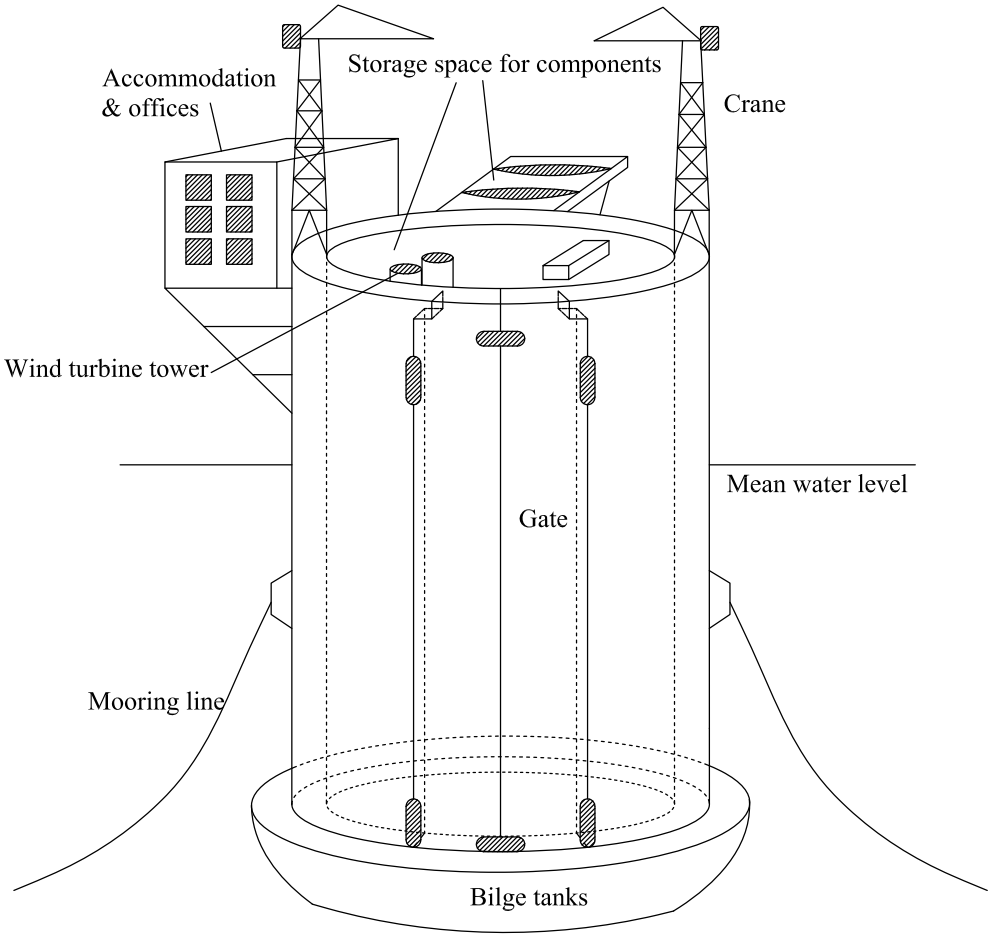

Fig. 1. Schematic of the floating dock concept.

The dock does not have any self-propulsion systems and should be wet-towed by tug boats during transit. During this phase, no spar inside is considered. Wind turbine components including blades, towers, and nacelles can be transported to offshore sites separately via barges. When the dock has moved on site, a distributed ballast system is activated to ballast the dock until a specified draft is reached. Then, the mooring system is deployed by anchor handlers before the installation crew is transferred to the dock preparing for installation tasks. In the next step, wind turbine components are transported from barges to storage space on the dock prior to installation of wind turbines.

For an offshore site, the dock is expected to stay on site and be manned until the whole wind farm is installed. The dock should be designed to survive extreme environmental conditions and other hazards.

When a wind farm project is finished using the dock, the decommissioning process of the dock resembles a reverse process of the installation procedure, and the de-ballasted dock can be transported to another offshore site for installation tasks or to shipyard for a scheduled maintenance.

2.3. Procedures for installing a spar floating wind turbine

Fig. 2 shows the proposed main steps for installing a spar FWT using the floating dock. Suppose that a spar foundation has been wet-towed to the site horizontally, the first step is to upend the spar foundation to a vertical position. Then, the gate at the dock side is opened, and the spar foundation is moved into the middle of the dock with the assistance of tug boats. In step 3, tugger lines are used to connect the spar foundation to the dock in order to avoid large drift-off of the spar in the horizontal plane. Step 4 is a key step, during which the tower, nacelle, and blades are individually mated and bolted onto each other. The mating processes between a tower and a spar foundation and between a blade and a hub are deemed critical events. Structural failures due to impact could occur to the guide pins if large relative motions between the mating parts exist [11]. When installations of the wind turbine components are finished, the spar foundation will be disconnected from the dock (step 5) and towed out of the dock to a designated location (step 6). Finally, pre-laid mooring lines are hooked up with the spar, and installation of the spar FWT is completed.

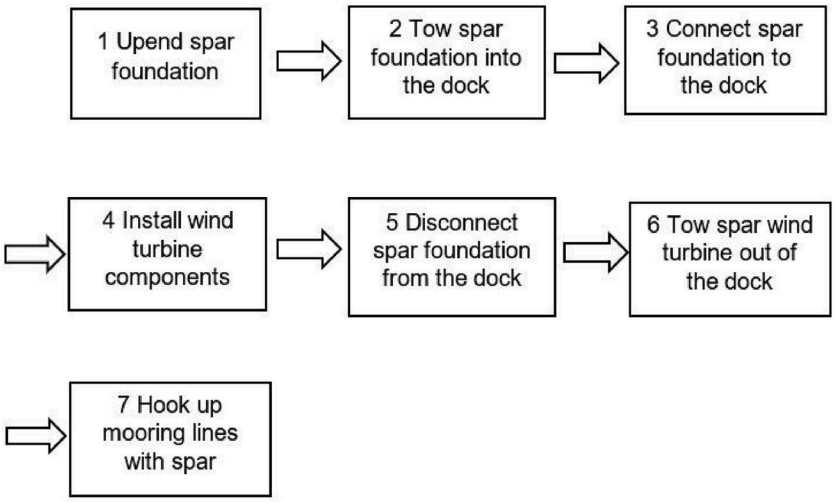

Fig. 2. Main installation steps of a spar floating wind turbine.

2.4. Design challenges

Design of the floating dock concept faces a few technical and economical challenges. The dimension of the dock should be sufficiently large to accommodate cranes, wind turbine components, living unit and other necessary facilities and to provide stability of the floating dock. Because of the moonpool inside the dock, piston-mode resonance and sloshing of the internal fluid can occur [21], and these phenomena may affect the motion performance of the dock and the spar during installation under certain sea states. If these hydrodynamic phenomena hinder the installation activity, alternative solutions should be considered. Structural design of the dock needs to address the large opening created by the gate, and internal reinforcement within the side walls is needed to avoid large structural deformation. Ultimate load analysis and fatigue check should be performed for main structural members after a detailed structural design is conducted. Additionally, the deck space and other storage areas should be properly utilised to accommodate a maximum number of wind turbine components. Economically, the dock should be designed with relatively low production, installation, and maintenance costs. Some of the design challenges are not addressed in this paper.

2.5. Design considerations

The shape of the floating dock is kept cylindrical for the sake of simplicity. Fig. 3 illustrates a side view of the dock in operational and transit conditions, and Table 1 summarises the 11 independent design variables considered. Some are related to hull form and

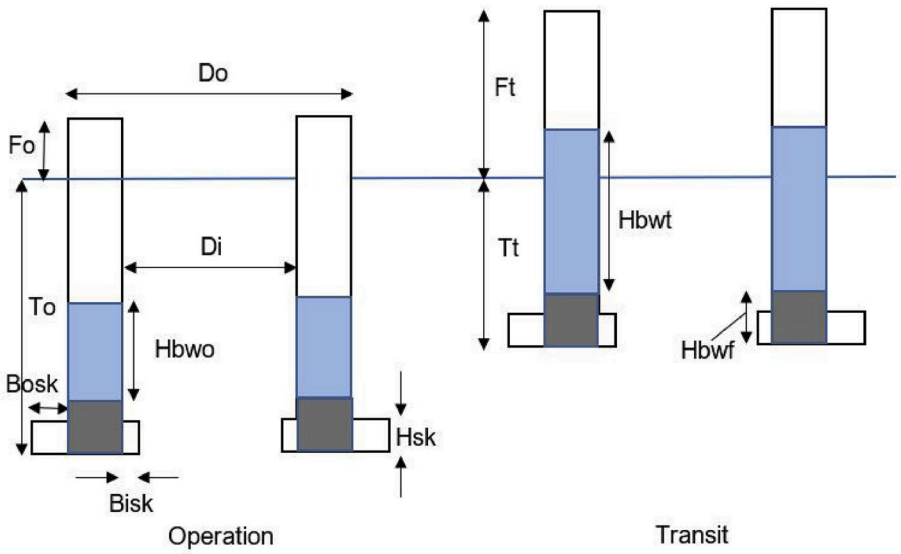

Fig. 3. Illustration of the design variables of the floating dock.

Table 1
Independent design variables.

Design variables	Symbols	Lower and upper bounds (m)
Dock outer diameter	*Do*	70 to 190
Dock inner diameter	*Di*	60 to 180
Dock draft in operation	*To*	65 to 100
Dock freeboard in operation	*Fo*	20 to 25
Dock draft in transit	*Tt*	5 to 20.1
Height of fixed ballast	*Hbf*	1 to 25
Height of water ballast in operation	*Hbwo*	not explicitly specified
Height of water ballast in transit	*Hbwt*	not explicitly specified
Outward extension of bilge tank	*Bosk*	6 to 15
Inward extension of bilge tank	*Bisk*	not explicitly specified
Height of bilge tank	*Hsk*	4 to 8

others are related to ballast. Note that the freeboard in transit, *Ft*, is a dependent variable and is not listed here. The current design parameters and constraints were chosen after several iterations with engineering experts through roundtable discussions. The lower bound of the inner diameter is determined considering that the diameter of a spar supporting a 10-MW (MW) wind turbine is around 14 m. The upper bound of the dock draft and outer diameter in transit is chosen to be the maximum draft and width of the Suez Canal. It is assumed that scrap steel can be used as fixed ballast which fills the bottom parts of the dock and the bilge tanks; see the grey area in Fig. 3. The fixed ballast and the water ballast are used to lower the centre of gravity of the dock to achieve adequate static stability.

For a design problem, realistic design constraints should be addressed. In the shape optimisation, we only consider preliminary design requirements for the floating dock rather than the accidental limit states (ALS), ultimate limit states (ULS), fatigue limit states (FLS), or serviceability limit states (SLS) [22]. These limit states are often required for a detailed design. Two linear constraints are proposed as follows:

1. Breadth of upper deck: $10 \leq Do - Di \leq 100$
2. Inward extension of bilge tank: $0 \leq Bisk \leq \frac{Di-Dspar}{2}$

These constraints can be expressed explicitly by linear combination of design variables and are due to physical limitations. The upper deck must be wide enough for storage and the inward extension must not interfere with the spar foundation during installation.

Additionally, the following eight nonlinear constraints are implemented:

1. Ballast water in operation ($0 \leq Hbwo + Hbf \leq To + Fo$)
2. Ballast water in transit ($0 \leq Hbwt + Hbf \leq Tt + Ft$).
3. Initial stability in operation ($GMo \geq 1.0$ m)
4. Initial stability in transit ($GMt \geq 1.0$ m)
5. Wind-induced heeling angle in operation ($\eta_5 o \leq 2$ deg)
6. Wind-induced heeling angle in transit ($\eta_5 t \leq 2$ deg)
7. Wind-induced heeling angle in survival condition ($\eta_5 s \leq 7$ deg)
8. Piston-mode resonance criterion in operation ($T_{piston} \geq 17$ s)

Among these, constraints 1 and 2 are due to physical limitation of the ballast water height, and constraints 3 and 4 are set up to satisfy the requirement of initial stability for offshore units [23,24]. Because the floating dock will be placed near an offshore wind farm for a long time in terms of several months, such operations can be considered as weather unrestricted [25]. Constraints 5, 6 and 7 are specified to achieve stringent stability requirement in all stages of operations. A wind speed of 36 m/s was selected for operation and transit, and 52 m/s for survival condition based on offshore standards [24]. These wind speeds are recommended for the check of intact stability of mobile offshore units, and actual wind speeds for installation of offshore wind turbines are much lower [26]. The maximum heeling angles in constraints 6 and 7 are conservative. Constraint 8 is set up to avoid excitation of the piston-mode resonance under sea states with low spectral peak periods (*Tp*). Here, Molin's formula (Eq. (1)) was implemented with a safety factor for estimating the resonance frequency. In Eq. (1), *g* is the constant of gravitational acceleration. Molin's formula was originally developed for estimating piston-mode resonance in a two-dimensional (2-D) moonpool between two hulls, but provides good accuracy for our cases after comparison with the hydrodynamic analysis results using WADAM [27]. In constraint 8, a lower bound of 17 s is chosen considering the operational sea states. This value, if further increased, results in greater dimensions of the dock. Other possible constraints are not considered. For example, the dynamic motion performance of the system will influence the limiting sea states of the dock, but it is not addressed here.

$$\omega_{piston} = \sqrt{\frac{g}{To(1 + Di(1.5 + \ln(Do/2Di))/\pi To)}} \tag{1}$$

Ideally, the design objective function of the dock should include material, production, maintenance and other costs during its

lifetime. For simplicity, only the material cost is considered here, and the objective function can be expressed as the total costs of individual plates. In this case, the components include the upper and lower decks, inner and outer walls, and plates of the bilge tanks. The costs of ballast water and other equipment do not depend on the design variables and thus are not considered in the objective function.

The dock design problem has a relatively simple objective function with complex constraints. In this work, the constrained nonlinear programming problem was solved using a gradient-based subroutine in Matlab 2016 [28]. During the design optimisation, assumptions are made regarding the weight and mass distribution of multiple modules based on experiences from offshore industry. In addition, five 10-MW wind turbines are assumed to be stored in the deck storage.

Details of the optimisation are not the focus of this paper. Table 2 lists main properties of the optimum dock. As shown, the

Table 2
Main particulars of the optimum dock.

Parameter	Symbol	Value
Outer diameter (m)	*Do*	80.3
Inner diameter (m)	*Di*	60
Height of fixed ballast (m)	*Hbf*	1.25
Outward extension of bilge box (m)	*Bosk*	6.0
Inward extension of bilge box (m)	*Bisk*	0.0
Height of bilge box (m)	*Hsk*	4.0
Steel weight	M_{st}	1.0566E4
Operational condition		
Draft (m)	*To*	65
Freeboard (m)	*Fo*	20
Height of ballast water (m)	*Hbwo*	48.54
Displacement (tonnes)	Δo	1.9687E5
Payload with 5 wind turbines (tonnes)	*Wo*	1.55E4
Vertical centre of gravity above keel (m)	*KGo*	28.54
Transit condition		
Draft in transit (m)	*Tt*	20
Freeboard (m)	*Ft*	65
Height of ballast water (m)	*Hbwt*	0.0
Displacement (tonnes)	Δt	9.3677E4
Vertical centre of gravity (COG) above baseline (m)	*KGc*	28.6
Payload (tonnes)	*Wt*	6000
Vertical centre of gravity above keel (m)	*KGt*	18.52

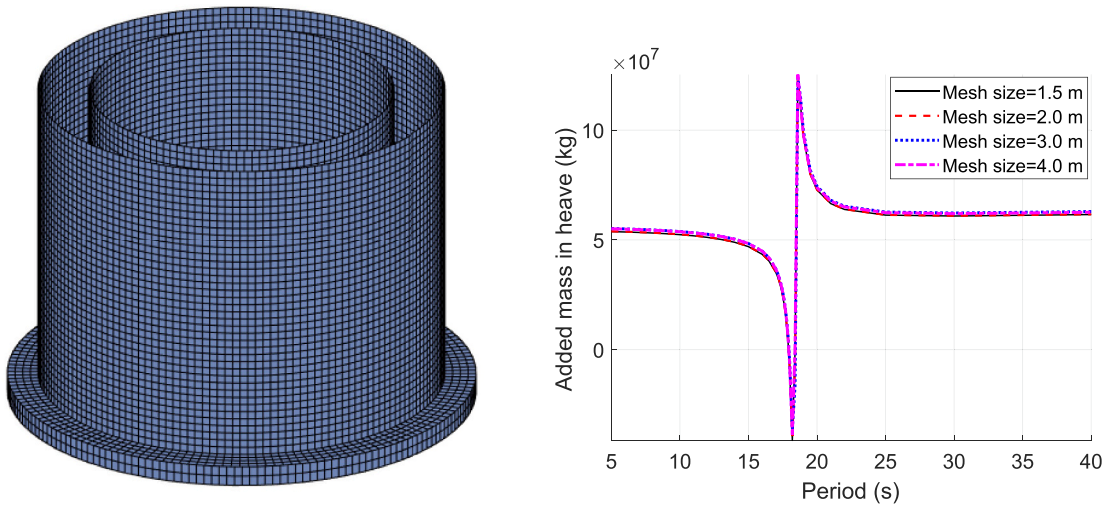

(a) Panel model of the optimal dock (Mesh size=1.5 m)

(b) Convergence of mesh size

Fig. 4. Sensitivity study on the mesh size in the hydrodynamic analysis.

displacement in operation reaches 196870 tonnes, and the displacement in transit reduces to 93677 tonnes. This optimum was verified by generation of random samples of design variables in a sensitivity study.

3. Hydrodynamic analysis

3.1. Hydrodynamic analysis of a single dock

After the design optimisation, hydrodynamic analysis of the dock was performed using the WADAM code [27]. WADAM provides the potential-flow solution to the diffraction/radiation problem using the boundary element method. In this work, the wetted area of the dock is meshed with low-order quadrilateral panels; see Fig. 4(a) for an illustration. To determine the panel size of the optimal dock, a convergence study on the panel size was conducted. Fig. 4(b) shows a comparison of the added mass in heave using four mesh sizes from 1.5 m to 4.0 m. The substantial oscillation in the added mass near a period of 18 s is due to the piston-mode resonance, which refers to an oscillating water mass flux with large amplitude. A mesh size of 2.0 m is deemed adequate and used in the hydrodynamic analysis. Sloshing exists for almost any structures containing a liquid with a free surface and can be the results of resonant excitation of the tank liquid. Potential flow theory of an incompressible liquid can adequately describe sloshing in many cases. For a 2-D tank illustrated in Fig. 5 (a), Faltinsen et al. [21] used separation of the two spatial variables y and z to solve the spectral boundary problem

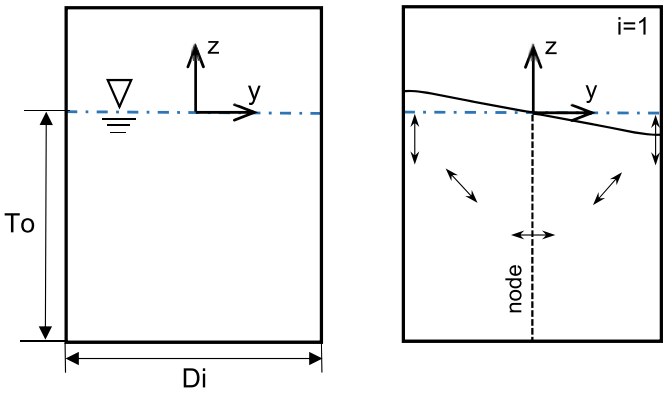

(a) Mean liquid shape and notations used for a 2-D tank (b) Standing wave corresponding to the first natural mode for sloshing

Fig. 5. Schematic of the linear natural sloshing modes.

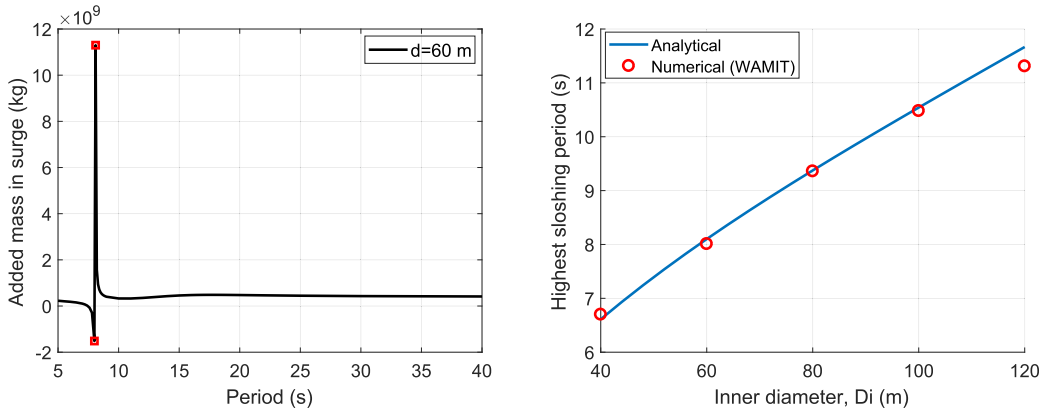

(a) (b)

Fig. 6. Slosing period predicted by numerical and analytical solutions (Eq. (2)).

and provided exact analytical natural modes and frequencies for sloshing. As shown in Fig. 5(b), the lowest linear mode is an anti-symmetric standing wave with wavelength twice the tank length; a liquid particle moves only horizontally along the nodal line. This mode corresponds to the highest natural period and is of prime importance in assessing the severity of sloshing. The general expression for natural sloshing periods is:

$$T_{sloshing,k} = \frac{2\pi}{\sqrt{2g\iota_{1,k}tanh(2\iota_{1,k}To/Di)/Di}} \tag{2}$$

where $T_{sloshing,k}$ denotes the sloshing frequency for the k-th mode, g is the constant of gravity acceleration, $\iota_{1,k}$ is k-th nondimensional root of the equation $J_1'(\iota_{1,k}) = 0$ where J_1 is the Bessel function of the first kind. In this case, Di and To refer to the inner diameter and operational draft of the dock, respectively. Although the dock under analysis is bottomless, the highest sloshing periods by the panel method agree well with those from Eq. (2). Fig. 6(a) demonstrates the oscillation in the surge added mass near a period of 8.1 s. Fig. 6 (b) presents a study using a constant height and a varying inner diameter. As indicated, the highest sloshing period increases monotonically with the inner diameter. This is because the highest natural period of the sloshing mode depends on the liquid-depth-to-tank-breadth ratio [21]. Unless a very large inner diameter is considered, the highest sloshing period is likely to fall in the range of wave periods (4–25 s).

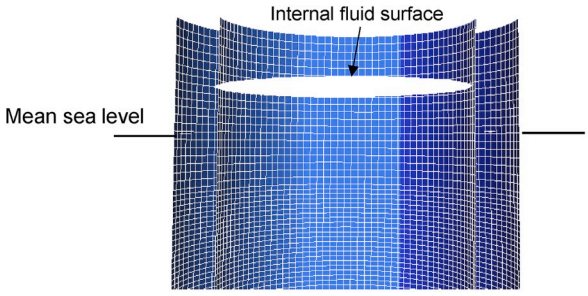

(a) Time instant I during a piston-mode cycle

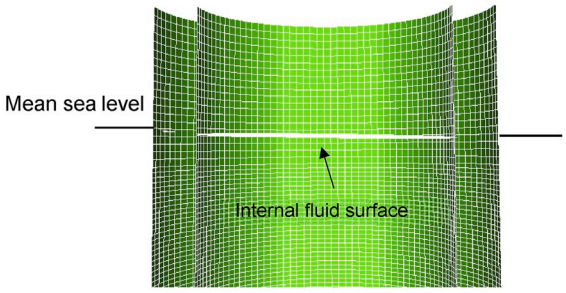

(b) Time instant II during a piston-mode cycle

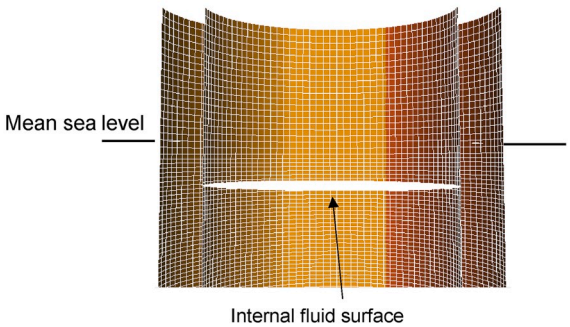

(c) Time instant III during a a piston-mode cycle

Fig. 7. 3-D visualisation of the piston-mode resonance (near T = 18 s) for the optimum dock.

3.2. Internal wave elevation inside the dock

To assess the resonant waves inside the floating dock, the potential-flow hydrodynamic analysis was carried out without consideration of the spar floater inside. Transfer functions of the internal wave elevation, water particle velocity or hydrodynamic pressure were obtained for specified field points. For the optimum dock (Table 2), a meshgrid of 60 × 60 field points was generated on the internal mean water surface, and 3-dimensional (3-D) visualisations of the fluid free surface during the piston-mode resonance and the linear sloshing are shown in Fig. 7 and Fig. 8, respectively. Here, time instant I, II, and III give three representative free surface snapshots during a cycle. For the piston-mode resonance, the internal free surface remains flat during an oscillation cycle. For sloshing, the shape of the standing wave resembles the one presented in Fig. 5.

Fig. 9(a) shows the position of three representative field points, where Point 1 is at the dock centre, Point 3 is close to the inner wall, and Point 2 is in between. In the hydrodynamic analysis, to reduce the resonant response in the moonpool, a damping lid can be added to account for viscous flow and separation [29]. The free surface mesh of the damping lid was created in HydroMesh [30] and illustrated in Fig. 9(b). This lid covers the internal waterplane of the dock. The transfer functions of the internal wave elevation per unit external incoming wave amplitude are presented in Fig. 10(a) and (b) for the undamped and damped cases, respectively. Because of its

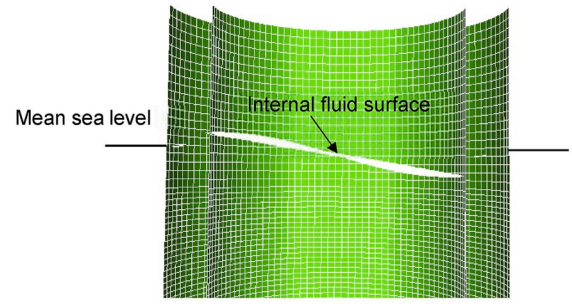

(a) Time instant I during a sloshing cycle

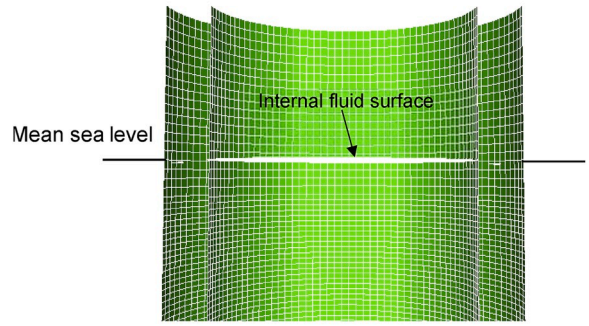

(b) Time instant II during a sloshing cycle

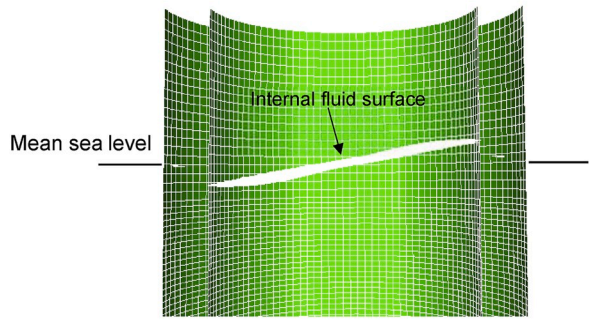

(c) Time instant III during a sloshing cycle

Fig. 8. 3-D visualisation of the linear sloshing phenomenon (near T = 8 s) for the optimum dock.

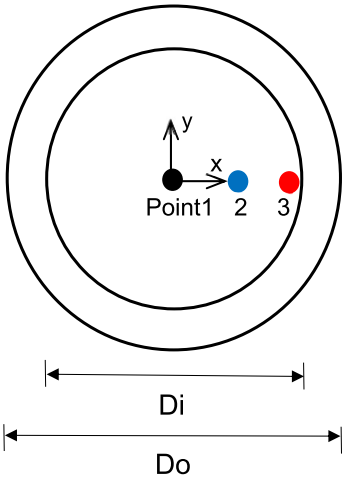

(a) Schematic of the selected field point positions

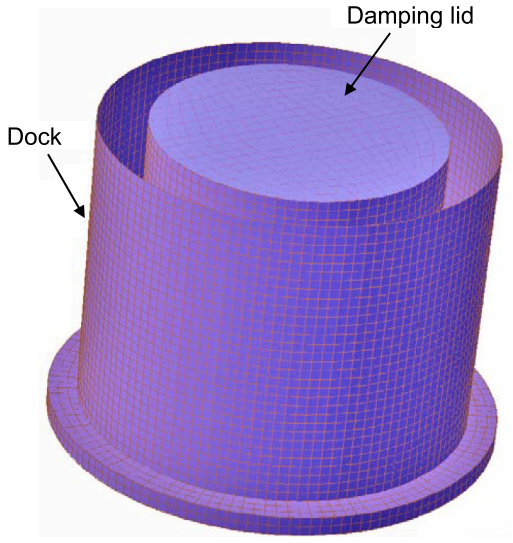

(b) Isometric veiw of the panel model with a damping lid

Fig. 9. Investigation of the internal wave elevation inside the optimum dock.

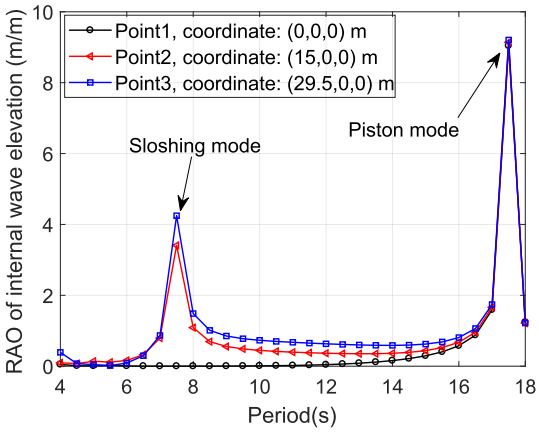

(a) Undamped, internal surface without damping lid

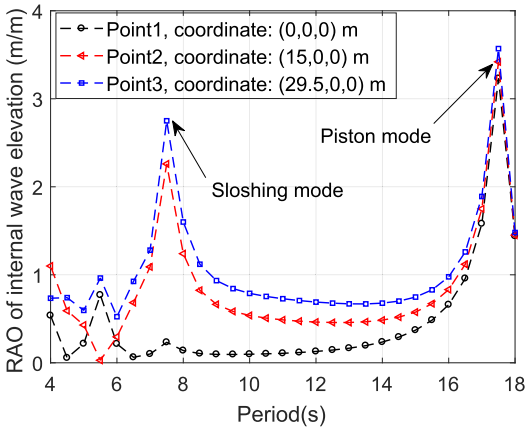

(b) Damping coefficient=0.02, internal surface with a damping lid

Fig. 10. RAO magnitude for the field points with different damping configurations.

symmetrical position, Point 1 does not exhibit the peak related to the linear sloshing mode in the response amplitude operator (RAO), and all three points have a prounced peak due to the piston-mode resonance. Compared to the undamped case, when a small linear damping coefficient of 0.02 is applied to the lid, the piston-mode peak and the sloshing-mode peak reduce by 62% and 35%, respectively. In Fig. 10(b), additional smaller spikes are observed between 4 and 6 s. These peaks are physical and correspond to the higher resonance modes captured by the free surface mesh [30]. The actual damping level should be calibrated with experiments or full-scale measurements, which are beyond the scope of this work. The RAO magnitudes will be applied in Sec. 6.5.4.

3.3. Coupled hydrodynamic analysis

Two-body hydrodynamic analysis of the optimum dock and a spar was also conducted considering the hydrodynamic coupling between the bodies. In this analysis, the spar centre is aligned with the dock centre with no external stiffness matrice specified. The coupled hydrodynamic coefficients for both dock and spars including added mass and radiation damping as well as the mean drift on the dock were further used in the dynamic response analysis in the time domain.

4. Preliminary design of the mooring system

A passive mooring system is proposed for the floating dock at a water depth of 200 m. The mooring system consists of four groups, and each group is a cluster of three lines with a spacing of 3 deg in between. Fig. 11(a) shows a schematic of the mooring composition. As shown, each mooring line is composed of wire ropes, chain links, and connecting links. Table 3 summarises the chosen properties

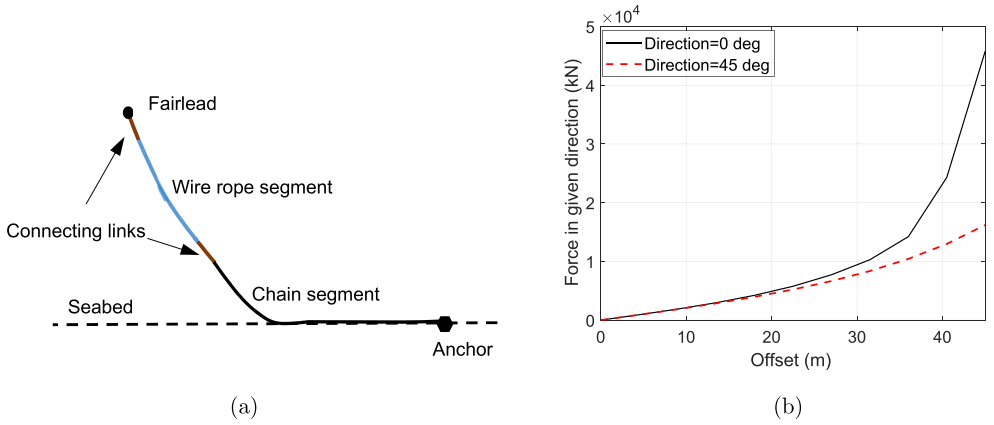

Fig. 11. Illustration of the mooring configuration and restoring curves.

Table 3
Selected properties of the mooring system under no environmental loads.

Parameter	Symbol	Value
Number of mooring lines (−)	N_{moor}	12
Total length of mooring line (m)	L_{tot}	660
horizontal distance from fairlead (m)	L_H	595
Length of wire rope (m)	L_w	185
Length of chain (m)	L_c	475
Diameter of wire (mm)	D_w	140
Diameter of chain (mm)	D_c	160
Unit submerged weight of wire (kN/m)	W_w	0.801
Unit submerged weight of chain (kN/m)	W_c	4.367
Axial stiffness per unit length of wire (kN)	EA_w	1.779E6
Axial stiffness per unit length of chain (kN)	EA_c	1.971E6
Breaking strength of wire (kN)	Tb_w	2.038E4
Breaking strength of chain (kN)	Tb_c	1.781E4
Pretension in the top segment (kN)	T_{pre}	1085.1
Angle at upper end from vertical (deg)	α_{moor}	43.2
Angle between lines in each group (deg)	θ_{moor}	3

which are determined after several iterations. The MIMOSA [31] software was used to check the static restoring characteristics; refer to Fig. 11(b)) for the total restoring forces provided by the 12 mooring lines in two directions. The present choice of mooring system is a simple solution for station-keeping of the dock in operational conditions. Detailed design optimisation of the mooring system is out of the scope of this work.

5. Description of the two spars

Two spar foundations are considered in this study, and Table 4 summarises the main parameters. Both foundations are designed to support 10-MW wind turbines and have a diameter of 14 m for the lower cylinder; see Fig. 12 for the submerged parts of the spars. Spar1 has a displacement of 1.5E4 tonnes, and Spar2 is longer with a displacement of 1.9E4 tonnes. In the numerical model in SIMO, the roll/pitch and heave damping of the spars are set as approximately 3% and 6% critical damping, respectively. These values were chosen based on knowledge of existing spars.

6. Dynamic response analysis of the coupled system

This paper emphasises the functionality of the concept and applies dynamic response analysis considering the SLS design requirement. Other limit states mentioned in Sec. 2.5 are not addressed. After mating with wind turbine components, the spar FWTs will have increased pitch and roll natural periods. Here, the focus is on motions of the spar foundations without rotor, nacelle, or tower. Numerical modelling and analysis is presented of the dock-spar systems. For comparison purposes, the hydrodynamic loads and motions of the single spars without the dock are used as references in the results.

Table 4
Selected parameters of the two spar foundations prior to installation of wind turbines.

Parameter	Symbol	Value
Spar1		
Total draft (m)	T_{s1}	96.3
Freeboard (m)	F_{s1}	10
Displacement (tonnes)	Δ_{s1}	1.4906E4
Vertical centre of gravity above keel (m)	KG_{s1}	24.22
Vertical centre of buoyancy above keel (m)	KB_{s1}	47.32
Spar2		
Total draft (m)	T_{s2}	133.6
Freeboard (m)	F_{s2}	10
Displacement (tonnes)	Δ_{s2}	1.8957E4
Vertical centre of gravity above keel (m)	KG_{s2}	30.66
Vertical centre of buoyancy above keel (m)	KB_{s2}	61.72

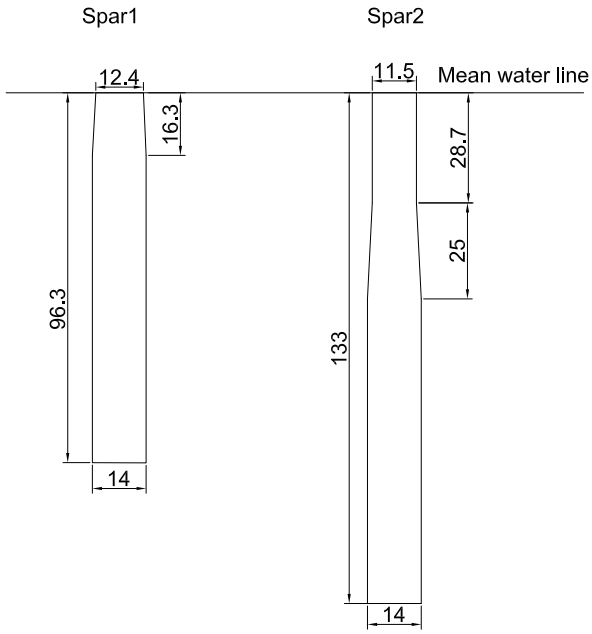

Fig. 12. Main dimensions of the two spars.

6.1. System description

Assuming that the spar foundation has already been placed inside the dock and connected to the dock via four tugger lines, we can model the coupled system numerically in SIMO [32]. SIMO is a numerical code developed by SINTEF Ocean AS and can compute the dynamic behaviour of multiple floating bodies under complex environments.

In this work, the system consists of the optimum dock and a spar foundation. They are connected via four horizontal springs at mean water level (Fig. 13), each spring has a linear stiffness of 2 kN/m. This level of stiffness was used to avoid large horizontal offset between the two floating bodies while keeping a soft mechanical coupling between the bodies. The dock is connected to the catenary mooring lines described in Sec. 4. To account for the viscous damping, Morison-type drag elements were distributed circumferentially along the bilge tanks in the numerical model.

For the dock with Spar1 or Spar2, the piston-mode resonance periods and the highest sloshing periods obtained from hydrodynamic analysis are listed in Table 5. For the given dimension of the optimium dock, the periods with either Spar1 or Spar2 are close and do not deviate much from the analytical estimates for 2-D cases.

6.2. Eigen value analysis

To evaluate the eigen properties of the rigid-body motions of the coupled system, eigen value analysis was conducted. The eigenmodes and natural periods were obtained by solving Eq. (3):

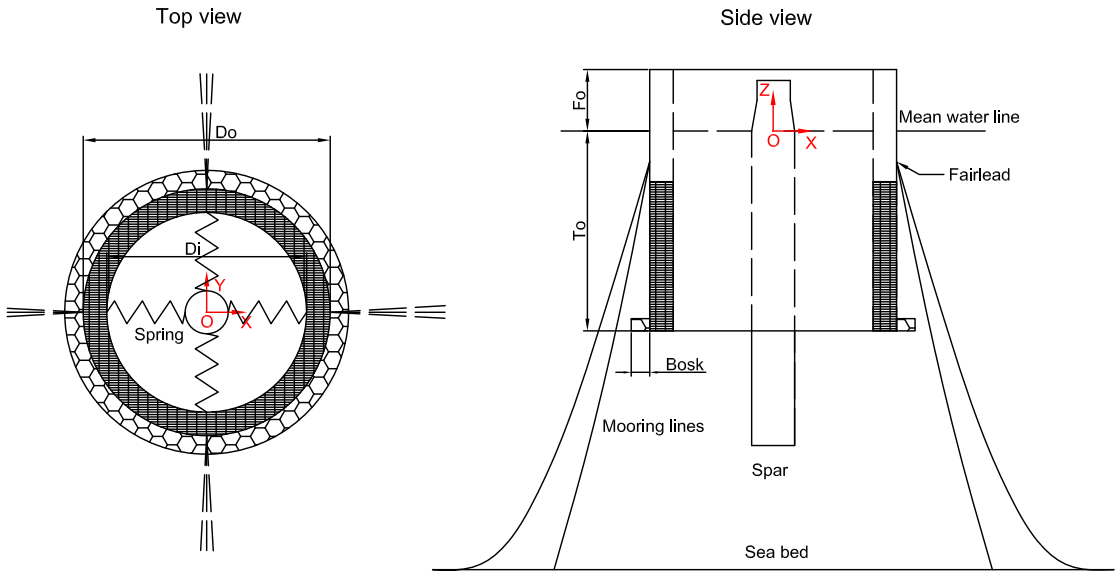

Fig. 13. Schematic of the dock system with mooring lines.

Table 5
Piston-mode and sloshing periods from hydrodynamic analysis.

Name	Symbols	Value (s)
Piston-mode period, 2-D moonpool, Eq. (1)	$T_{piston0}$	18.6
Piston-mode period, dock with spar1	$T_{piston1}$	18.4
Piston-mode period, dock with spar2	$T_{piston2}$	18.3
Highest sloshing period, 2-D tank; Eq. (2)	$T_{sloshing0}$	8.1
Highest sloshing period, dock with spar1	$T_{sloshing1}$	8.5
Highest sloshing period, dock with spar2	$T_{sloshing2}$	8.3

$$\left[-\omega^2(\mathbf{M}+\mathbf{A})+\mathbf{C}\right]\cdot\mathbf{X}=0 \tag{3}$$

where ω is the natural frequency, and **M** is the mass matrix of the dock and spar foundation. **A** is the frequency-dependent added mass matrix, and **C** is the total restoring stiffness matrix, which is split into hydrostatic restoring, mooring restoring, and mechanical coupling between the dock and spar. **X** is the eigenvector that represents rigid-body motions, with six DOFs for the floating dock and six DOFs for the spar.

Tables 6 and 7 show the eigenmodes and natural (eigen) periods of the coupled system 1 and coupled system 2, respectively. The eigenmodes represent the relative motions of the DOFs. In either table, each column gives a mode shape of the system and the corresponding natural period. For instance, the fourth natural period is 19.3 s in Table 6. In this column, "-1" exists for the dock heave DOF and "0" exists for the other DOFs. This mode shape has a pure heave mode, as the dock is only offset by 1 m in the negative *z*-direction and all other DOFs are fully constrained. In comparison, some mode shapes have multiple nonzero elements, indicating coupling between different DOFs. Take the third mode in Table 6. Because "1" is registered for both the spar surge and pitch DOFs while other DOFs have negligible values, the spar has 1-m surge displacement and 1-deg rotation about the rotation centre at the mean water level for this system mode with a natural period of 18.98 s. For system 2, the natural period of this coupled mode rises to 22.1 s. As shown by the fifth mode in Table 6 and the seventh mode in Table 7, the heave DOFs of the spars are not coupled with other DOFs. Thus, Spar1 and Spar2 have a heave natural period of 22.8 s and 27.5, respectively. The surge, sway, and yaw natural periods of the dock are long because of the large mass of the floating system and the relatively low restoring stiffness provided by the mooring system.

6.3. Motion response amplitude operators of the spars

To evaluate the effect of the dock on the motion RAOs of the spar, we study the spar motions in the frequency domain. For a free-floating rigid body, the equation of motion can be expressed as [33].

Table 6
Natural periods and eigenmodes of rigid body motions of coupled system 1.

Body	Unit	1	2	3	4	5	6	7	8	9	10	11	12
Dock, surge	m	0.00	0.00	0.00	0.00	0.00	0.57	−0.47	0.00	**1.00**	−0.05	−0.02	0.05
Dock, sway	m	0.00	0.00	0.00	0.00	0.00	−0.47	−0.57	0.00	0.05	**1.00**	0.05	0.02
Dock, heave	m	0.00	0.00	0.00	**−1.00**	0.00	0.00	0.00	0.00	0.00	0.00	0.00	0.00
Dock, roll	deg	0.00	0.00	0.00	0.00	0.00	0.82	**1.00**	0.00	0.00	0.01	0.00	0.00
Dock, pitch	deg	0.00	0.00	0.00	0.00	0.00	**1.00**	−0.82	0.00	−0.01	0.00	0.00	0.00
Dock, yaw	deg	0.00	0.00	0.00	0.00	0.00	0.00	0.00	**−1.00**	0.00	0.00	−0.00	0.00
Spar1, surge	m	0.00	0.02	**1.00**	0.00	0.00	0.00	0.00	0.00	−0.84	0.04	−0.33	**1.00**
Spar1, sway	m	0.00	**−1.00**	0.02	0.00	0.00	0.00	0.00	0.00	−0.04	−0.84	**1.00**	0.33
Spar1, heave	m	0.00	0.00	0.00	0.00	**1.00**	0.00	0.00	0.00	0.00	−0.00	0.00	0.00
Spar1, roll	deg	0.00	**1.00**	−0.02	0.00	0.00	0.00	0.00	0.00	0.00	−0.01	0.00	0.00
Spar1, pitch	deg	0.00	0.02	**1.00**	0.00	0.00	0.00	0.00	0.00	0.01	0.00	0.00	0.00
Spar1, yaw	deg	**1.00**	0.00	0.00	0.00	0.00	0.00	0.00	0.00	0.00	0.00	0.00	0.00
Eigen-period	s	9.04	18.98	18.98	19.30	22.79	26.35	26.40	137.93	378.99	379.00	573.65	573.68

Table 7
Natural periods and eigenmodes of rigid body motions of coupled system 2.

Body mode	Unit	1	2	3	4	5	6	7	8	9	10	11	12
Dock, surge	m	0.00	0.00	0.00	0.00	−0.53	0.43	0.00	0.00	**1.00**	0.08	−0.05	0.00
Dock, sway	m	0.00	0.00	0.00	0.00	0.43	−0.53	0.00	0.00	0.08	**−1.00**	0.00	−0.05
Dock, heave	m	0.00	**−1.00**	0.00	0.00	0.00	0.00	0.00	0.00	0.00	0.00	0.00	0.00
Dock, roll	deg	0.00	0.00	0.00	0.00	−0.81	**1.00**	0.00	0.00	0.00	−0.01	0.00	0.00
Dock, pitch	deg	0.00	0.00	0.00	0.00	**−1.00**	−0.81	0.00	0.00	−0.01	0.00	0.00	0.00
Dock, yaw	deg	0.00	0.00	0.00	0.00	0.00	0.00	0.00	**1.00**	0.00	0.01	0.00	0.00
Spar2, surge	m	0.00	0.00	0.00	**−1.00**	−0.01	−0.01	0.00	0.00	−0.71	−0.05	**−1.00**	−0.02
Spar2, sway	m	0.00	0.00	**−1.00**	0.00	0.01	−0.01	0.00	0.00	−0.05	0.71	0.02	**−1.00**
Spar2, heave	m	0.00	0.00	0.00	0.00	0.00	0.00	**−1.00**	0.00	0.00	0.00	0.00	0.00
Spar2, roll	deg	0.00	0.00	**0.69**	0.00	0.00	0.01	0.00	0.00	0.00	0.01	0.00	0.00
Spar2, pitch	deg	0.00	0.00	0.00	**0.69**	−0.01	0.00	0.00	0.00	0.01	0.00	0.00	0.00
Spar2, yaw	deg	**1.00**	0.00	0.00	0.00	0.00	0.00	0.00	0.00	0.00	0.00	0.00	0.00
Eigen-period	s	9.02	19.32	22.11	22.11	27.12	27.15	27.47	137.93	405.47	405.48	642.94	642.97

$$[(\mathbf{M}+\mathbf{A}(\omega)]\ddot{\mathbf{x}}+[\mathbf{B}(\omega)+\mathbf{B}_{\mathbf{v}}]\dot{\mathbf{x}}+\mathbf{C}\mathbf{x}=\mathbf{F}(\omega) \tag{4}$$

where ω is the circular frequency, $\mathbf{x}$, $\dot{\mathbf{x}}$, and $\ddot{\mathbf{x}}$ are the displacement, velocity, and acceleration vectors, $\mathbf{M}$ is the mass matrix, $\mathbf{A}$ is the added mass matrix, $\mathbf{B}$ is the radiation damping matrix, $\mathbf{B}_{\mathbf{v}}$ is the linearised viscous damping matrix, $\mathbf{C}$ is the hydrostatic restoring stiffness matrix, and $\mathbf{F}(\omega)$ is the harmonic excitation force. For simplicity, $\mathbf{B}_{\mathbf{v}}$ can be taken as a fraction of the critical damping $\mathbf{B}_{\mathbf{crit}}$ as follows

$$\mathbf{B}_{\mathbf{v}}=\xi\mathbf{B}_{\mathbf{crit}} \tag{5}$$

If we assume that the incoming wave elevation is $\zeta=\zeta_a e^{i\omega t}$, $\mathbf{F}(\omega)$ is proportional to ζ, and x is expressed by $ae^{i\omega t}$, then the RAO is

$$RAO(\omega)=\frac{a}{\zeta_a}=\left\{-\omega^2[\mathbf{M}+\mathbf{A}(\omega)]+\mathbf{i}\omega[\mathbf{B}(\omega)+\mathbf{B}_{\mathbf{v}}]+\mathbf{C}\right\}^{-1}\cdot\mathbf{F}_0 \tag{6}$$

Eqs. (4)–(6) apply to a single spar with six DOFs or a spar-dock system with 12 DOFs. After specifying a B_{v55} (linearised pitch damping) of 3% critical and a B_{v33} (linearised heave damping) of 6% critical for both spars, with or without the dock, we computed the spar RAOs in WADAM. As shown in Fig. 14, the largest peaks correspond to the natural periods of the two spars, and Spar2 has higher heave and pitch natural periods than Spar1. The presence of the dock creates additional peaks in the heave and pitch RAOs, corresponding to the piston-mode resonance and sloshing resonance, respectively. For the heave RAO, the piston-mode peak induced by the dock indicates increased heave motions of the spars for wave periods from 15 to 20 s. The effect of the dock on the RAOs appears also significant when the period is lower. For periods between 4 and 10 s, the heave RAOs of the spars with the dock are one to two orders smaller than those of the single spars, but the differences are hard to observe in Fig. 14(a) because of the large peaks. For the pitch RAO, the dock results in a general reduction in the RAO magnitude of both spars when the period is below 15 s, except for the sloshing mode. Although this comparison considers only the hydrodynamic coupling and ignores the mechanical coupling described in Sec. 6.1, the influence of the dock on the spar motions is visible.

6.4. Time-domain simulation

To evaluate the motion performance of the dock and spar with couplings, numerical simulations were performed in the time domain using SIMO. For a rigid floating body with six DOFs, the equation of motion can be written in the time domain as

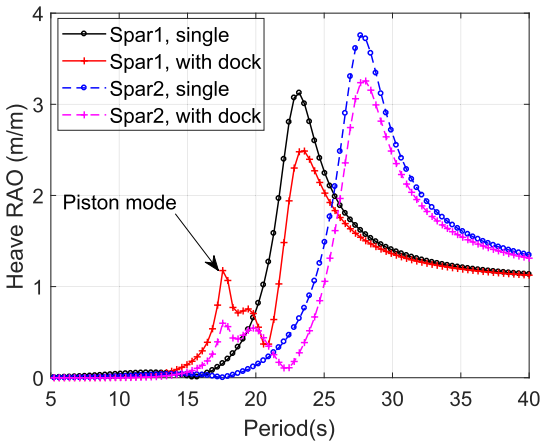

(a) Magnitude of the heave RAO of Spar1 and Spar2

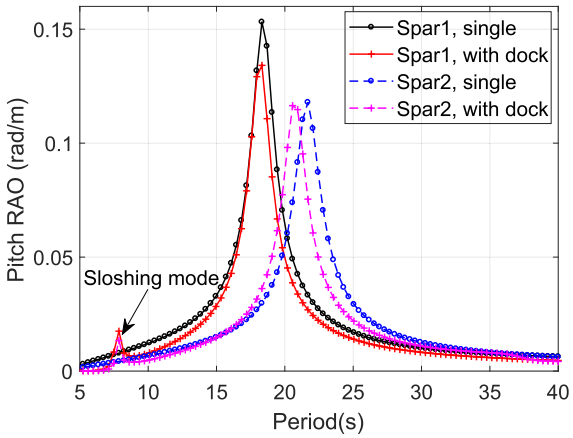

(b) Magnitude of the pitch RAO of Spar1 and Spar2

Fig. 14. Comparion of the spar RAOs with and without the optimum dock.

$$[(\mathbf{M}+\mathbf{A}(\infty)]\ddot{\mathbf{x}}\left(\mathbf{t}\right)+\mathbf{B}\dot{\mathbf{x}}\left(\mathbf{t}\right)+\int_0^{\mathbf{t}}\mathbf{k}\left(\mathbf{t}-\tau\right)\dot{\mathbf{x}}\left(\tau\right)\mathbf{d}\tau+\mathbf{C}\mathbf{x}\left(\mathbf{t}\right)=\mathbf{f}\left(\mathbf{t},\mathbf{x},\dot{\mathbf{x}}\right) \tag{7}$$

where $\mathbf{x}$, $\dot{\mathbf{x}}$, and $\ddot{\mathbf{x}}$ are the displacement, velocity, and acceleration vector in the time domain, respectively; $\mathbf{A}(\infty)$ is the added mass matrix at infinite frequency; $\mathbf{B}$ is the linearised viscous damping coefficients matrix; $\mathbf{k}(\tau)$ is the retardation function matrix calculated using the added mass and potential damping matrices; $\mathbf{C}$ is the restoring stiffness matrix, and $\mathbf{f}(\mathbf{t},\mathbf{x},\dot{\mathbf{x}})$ is the summation of the external force vector. The equation of motion of the coupled dock-spar system has 12 DOFs considering the two rigid bodies. In the simulations, the wave excitation forces include the Froude-Kryloff and diffraction forces, which are calculated by the panel method described in Sec 3. Based on Eq. (7), the equation of motion can be expanded and rewritten for the coupled system as

$$\begin{aligned}&\begin{bmatrix}(\mathbf{M}+\mathbf{A}(\infty))_{11} & \mathbf{A}(\infty)_{12}\\ \mathbf{A}(\infty)_{21} & (\mathbf{M}+\mathbf{A}(\infty))_{22}\end{bmatrix}\begin{bmatrix}\ddot{\mathbf{x}}_1(\mathbf{t})\\ \ddot{\mathbf{x}}_2(\mathbf{t})\end{bmatrix}+\begin{bmatrix}\mathbf{B}_{11} & 0\\ 0 & \mathbf{B}_{22}\end{bmatrix}\begin{bmatrix}\dot{\mathbf{x}}_1(\mathbf{t})\\ \dot{\mathbf{x}}_2(\mathbf{t})\end{bmatrix}\\ &+\int_0^t\begin{bmatrix}\mathbf{k}_{11}(\mathbf{t}-\tau) & \mathbf{k}_{12}(\mathbf{t}-\tau)\\ \mathbf{k}_{21}(\mathbf{t}-\tau) & \mathbf{k}_{22}(\mathbf{t}-\tau)\end{bmatrix}\begin{bmatrix}\dot{\mathbf{x}}_1(\tau)\\ \dot{\mathbf{x}}_2(\tau)\end{bmatrix}d\tau+\begin{bmatrix}\mathbf{C}_{11} & 0\\ 0 & \mathbf{C}_{22}\end{bmatrix}\begin{bmatrix}\mathbf{x}_1(\mathbf{t})\\ \mathbf{x}_2(\mathbf{t})\end{bmatrix}\\ &=\begin{bmatrix}\mathbf{f}_1^1(\mathbf{t})\\ \mathbf{f}_2^1(\mathbf{t})\end{bmatrix}+\begin{bmatrix}\mathbf{f}_1^2(\mathbf{t})\\ \mathbf{f}_2^2(\mathbf{t})\end{bmatrix}+\begin{bmatrix}\mathbf{f}_1^{\mathbf{drag}}(\mathbf{t})\\ 0\end{bmatrix}+\begin{bmatrix}\mathbf{f}_1^{\mathbf{coupling}}(\mathbf{t},\mathbf{x})\\ \mathbf{f}_2^{\mathbf{coupling}}(\mathbf{t},\mathbf{x})\end{bmatrix}\end{aligned} \tag{8}$$

where subscript 1 or 11 denotes the variables of body 1 (dock); subscript 2 or 22 denotes the variables of body 2 (spar); subscript 12 or 21 signifies the coupling terms between the bodies. The heave damping of the dock and spar are modelled by the linear damping matrix on the left-hand side of Eq. (8), whereas the drag forces on the bilge tanks are represented by the drag term on the right-hand side; $\mathbf{f}_1^1(\mathbf{t})$ and $\mathbf{f}_1^2(\mathbf{t})$ are the first- and second-order wave forces applied on the dock, respectively. $\mathbf{f}_1^{\mathbf{coupling}}(\mathbf{t},\mathbf{x})$ and $\mathbf{f}_2^{\mathbf{coupling}}(\mathbf{t},\mathbf{x})$ are the total mechanical coupling forces between the two bodies due to the springs (Fig. 13). As shown in the equation, hydrodynamic coupling between the dock and spar exists because of the coupled added mass and retardation function. For numerical integration of Eq. (8) in the time domain, the third-order Runge-Kutta method was applied with a time step of 0.1 s. Although sea states suitable for marine operations have relatively low *Tp* ranging from 4 to 10 s [34], we extend *Tp* to 16 s in order to capture the effect of Swell. Because this study focuses on operational conditions, two typical *Hs* of 1 and 2 m were considered in the simulations. As the dock is intended for global deployment, the single-peaked Pierson-Moskowitz (PM) spectrum [35] was applied to generate irregular waves for simplicity. A constant index ($n = 3$) was used for the spreading function cos^n of the short-crested waves [35], and the wave direction is in the negative *x*-direction (Fig. 13). For each combination of *Hs* and *Tp*, twenty 1800-s numerical simulations with random seed numbers were conducted to capture the stochastic nature of the wave processes, assuming that 1800 s is sufficient for carrying out the mating process.

6.5. Results and discussion

In this section, selected responses from the time-domain simulations are presented and discussed. The time series and spectra focus on two representative sea states with $Tp = 8$ s and $Tp = 16$ s, and the statistical results cover all simulations. Motions are addressed of the spar top (10 m above mean water level).

6.5.1. Time series of motion responses

Figs. 15 and 16 show time series of the wave elevation and heave and pitch motions of Spar1 under two different *Tp* and the same *Hs*. When $Tp = 8$ s, the dock has negligible dynamic motions, and Spar1 has relatively small motions with or without the dock. For the Spar1-alone case, the maximum pitch motion exceeds 0.5 deg and the maximum heave motion exceeds 0.02 m. The presence of the dock exerts a positive influence on motion reduction of Spar1–the maximum heave motion is kept well below 0.01 m and the maximum pitch motion is below 0.3 deg in Fig. 15. For $Hs = 2$ m, when *Tp* increases to 16 s, the influence of the dock appears to be negative. As shown in Fig. 16, the maximum heave motion of the dock exceeds 1 m, and the maximum heave motion of Spar1 exceeds 0.5 m. Because this wave period is close to the heave natural period of the dock (19.3 s), large heave motion of the dock is expected. The large heave motion of Spar1 is primarily due to the piston-mode excitation and is similar to that of Spar1 without the dock. Although the dock has small pitch motions, the maximum pitch motion of Spar1 approaches 3 deg and is comparable to that of Spar1 alone. Such a pitch magnitude is primarily due to the dock surge motions and the induced sloshing effect of the fluid inside the dock, and this effect is significantly reduced when the dock motions are constrained during simulations; see Fig. 17 for a comparion of the pitch motion of Spar1 when the dock is free-floating or constrained in six DOFs.

Figs. 18 and 19 present time series of the responses for Spar2 with and without the dock. Although Spar2 has a deeper draft and higher natural periods in heave and pitch than Spar1, the observation from the time series is similar. The dock appears to excert a

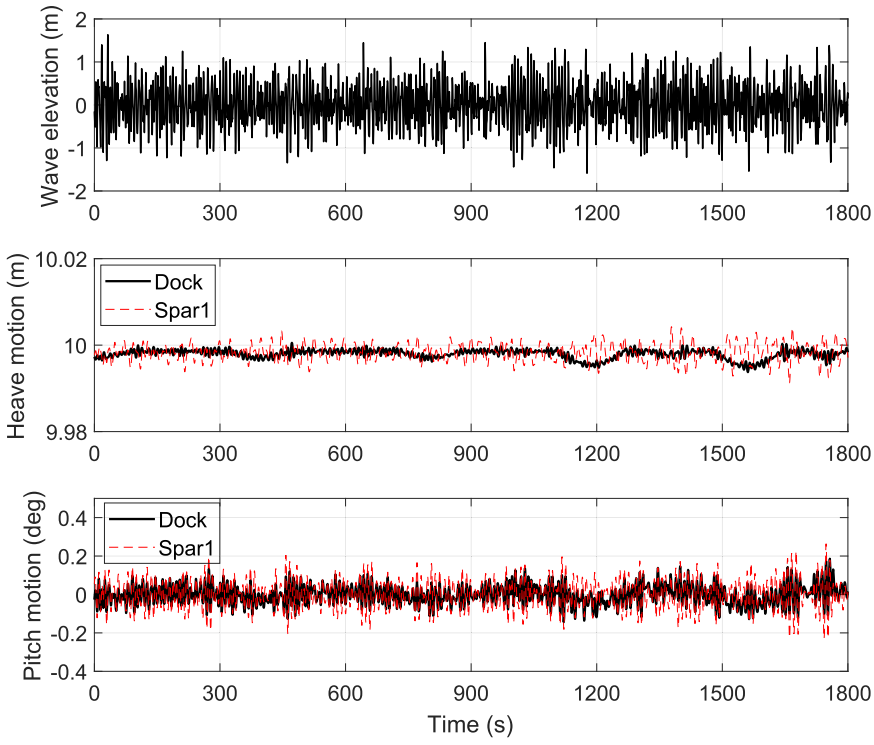

(a)

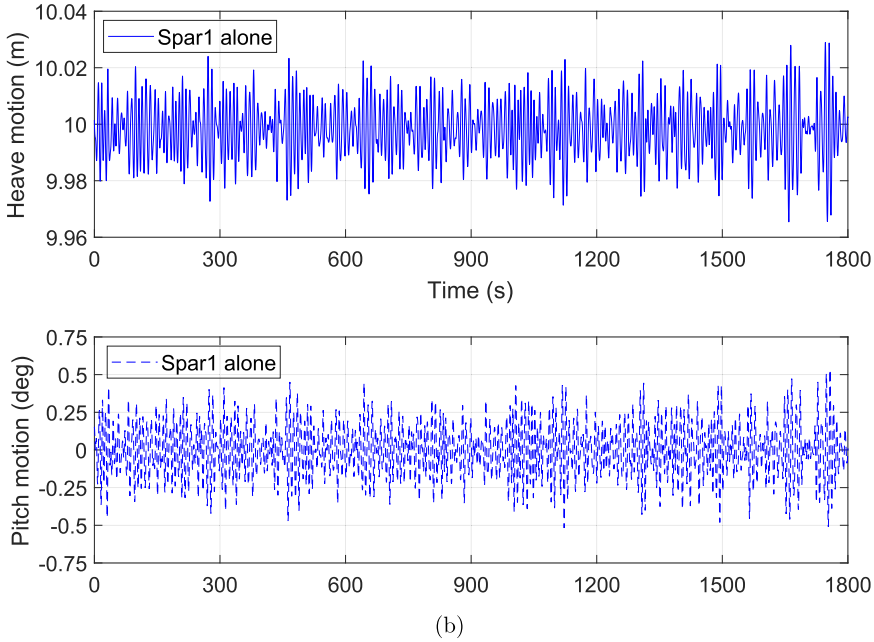

(b)

Fig. 15. Time series of numerical simulation of Spar1, $H_s = 2.0$ m, $T_p = 8$ s, Seed No.1.

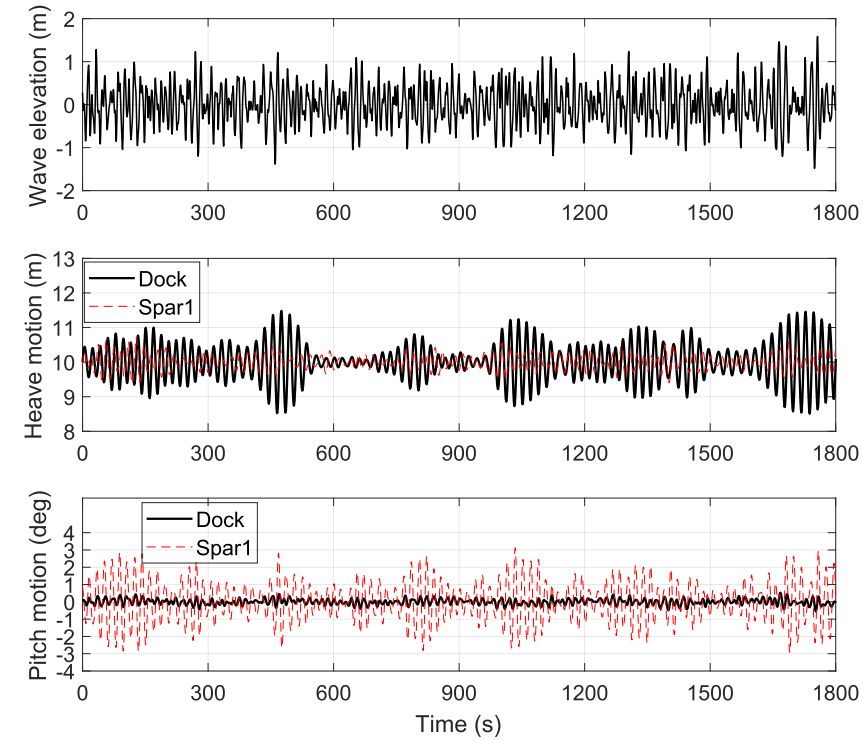

(a)

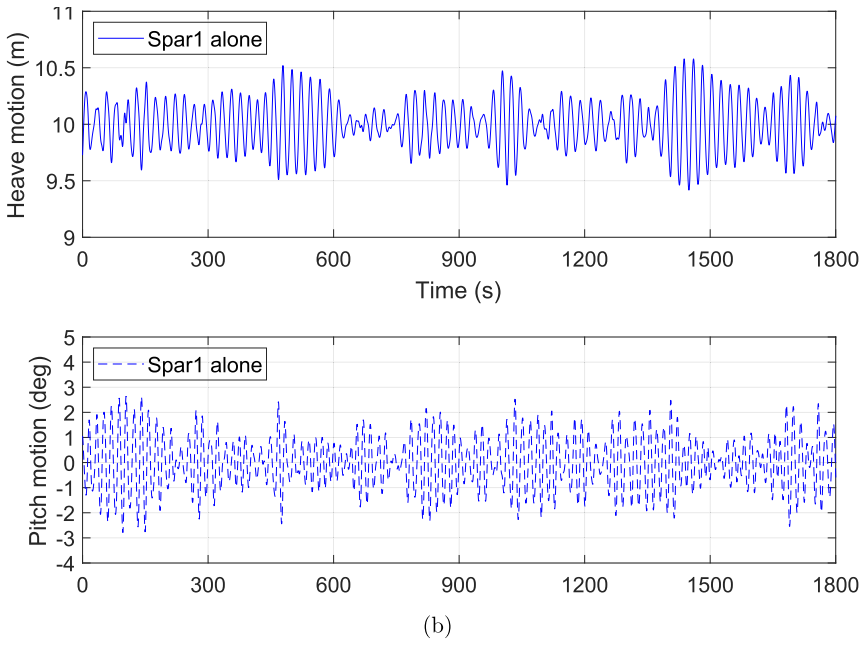

(b)

Fig. 16. Time series of numerical simulation of Spar1, $H_s = 2.0$ m, $T_p = 16$ s, Seed No.1.

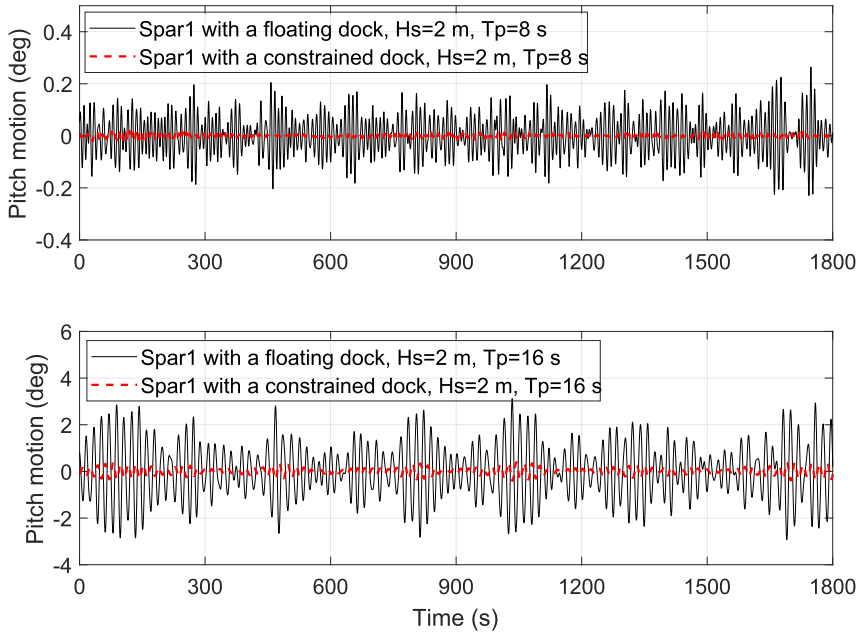

Fig. 17. Platform-pitch motion of Spar1 with the dock in free-floating and 6-DOF constrained conditions.

positive effect on the motion responses of Spar2 under $Tp = 8$ s, and the effect becomes slightly negative under $Tp = 16$ s, too. Compared with Spar1, Spar2 experiences reduced motions under both sea states.

6.5.2. *Spectra of wave forces and motion responses*

Figs. 20 and 21 show spectra of the surge and pitch wave excitation forces on the spars. These spectra were obtained from fast Fourier transform of the original time series. For $Tp = 8$ s and the case of Spar1 with dock, a peak in the spectral density of the surge excitation force can be observed near 0.77 rad/s which corresponds to the linear sloshing mode. However, the magnitude of this peak is relatively small compared to that of the spar-alone case; see Fig. 20(a). In this condition, Spar1 has visible heave excitations when exposed to open seas, but has negligible heave excitation forces when the dock is used. When Tp reaches 16 s, the wave length is close to 400 m, and because a portion of Spar1 (approximately 31 m) extends out of the dock bottom, there will be minor surge excitation force acting on Spar1, as shown in Fig. 20(b). In contrast, the heave excitation force is significant and overshadows the wave force of the spar-alone case. Such a large excitation is due to piston-mode resonance which occurs near 18.2 s. It is expected that substantial heave motion of spar will occur consequently. For Spar2, the observations of the spectra of the surge and heave excitation forces is similar to those of Spar1. Because Spar2 is more than 37 m longer than Spar1, the magnitude of the surge force spectrum is greater (Fig. 21(b)).

Motion response spectra of the spars with and without the dock are presented in Figs. 22 and 23. For $Tp = 8$ s, the dock shields Spar1 and Spar2 from first-order wave excitations and effectively reduce the wave-frequency responses which correspond to the greatest peaks in Figs. 22(a) and 23(a). The pitch motion responses of the spars due to sloshing inside the dock are less significant compared to those in spar-only conditions. Note that the integrated area of a motion spectrum equals the variance of a motion response. The absolute reduction in the reponse variance should be modest because of the relatively small responses of the spars under the sea state. For $Tp = 16$ s, because of the piston-mode excitations, the presence of the dock is likely to induce greater heave motion responses on the spars. As shown in Figs. 22(b) and 23(b), the heave response spectrum of Spar1 or Spar2 with the dock has two peaks. The smaller peak on the left corresponds to the wave-frequency response, and the larger peak on the right is due to the piston-mode excitation. In comparison, the influence of the dock on the pitch motion responses of the spars is less significant.

6.5.3. *Statistical results of motion responses*

The statistical results are presented in terms of the most probable maxima (MPMs). Each MPM is obtained using a Gumbel fit of 20 individual maxima and corresponds to the probability of non-exceedance of 37% in the cumulative distribution function [36]. The

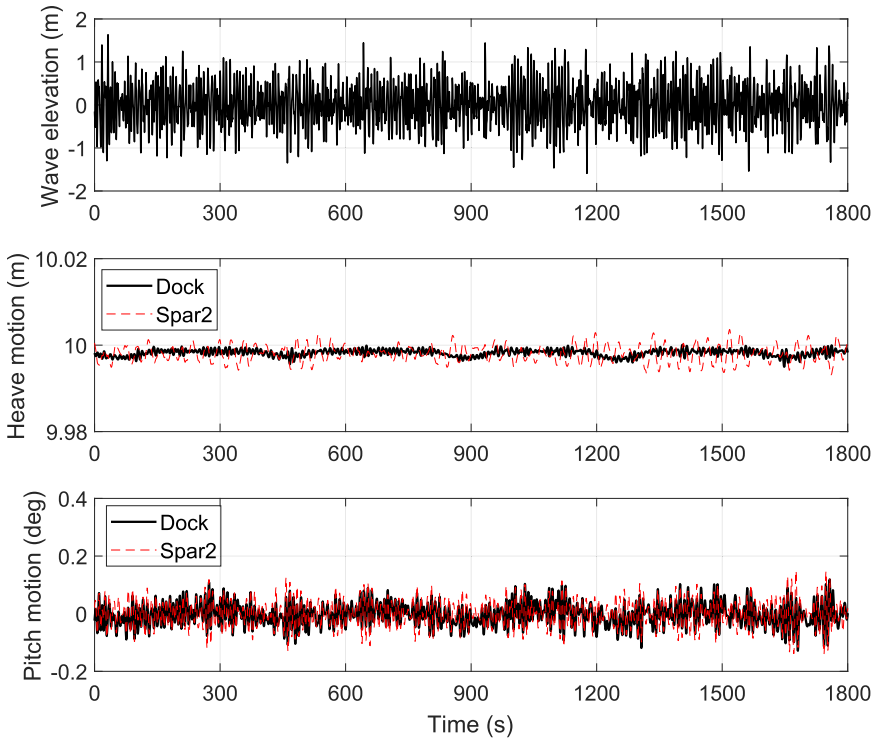

(a)

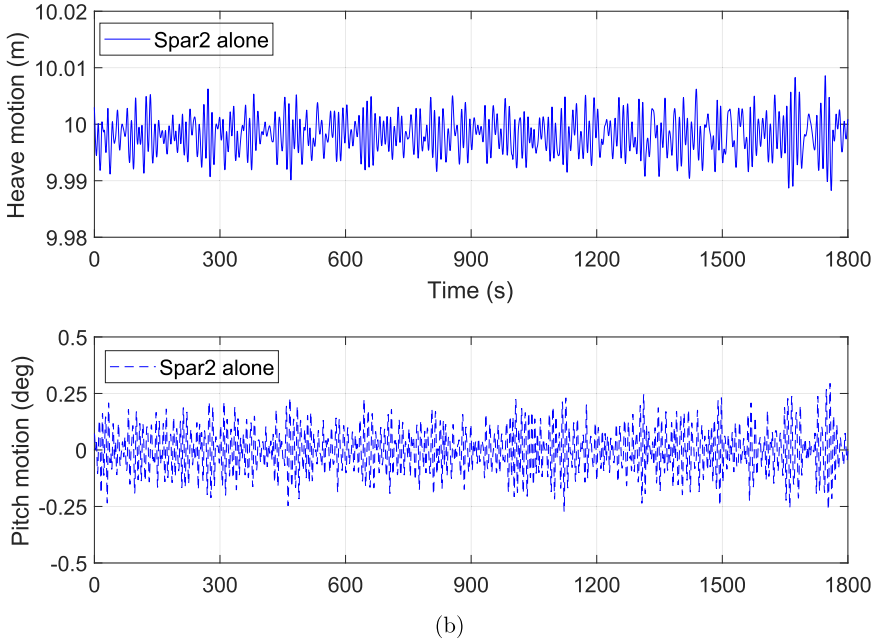

(b)

Fig. 18. Time series of numerical simulation of Spar2, $H_s = 2.0$ m, $T_p = 8$ s, Seed No.1.

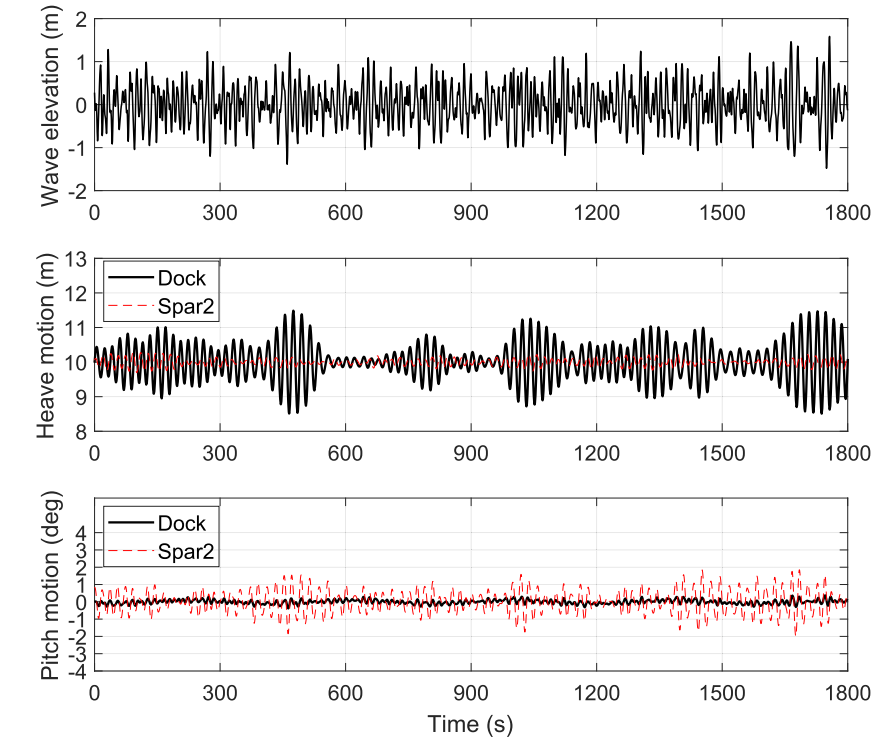

(a)

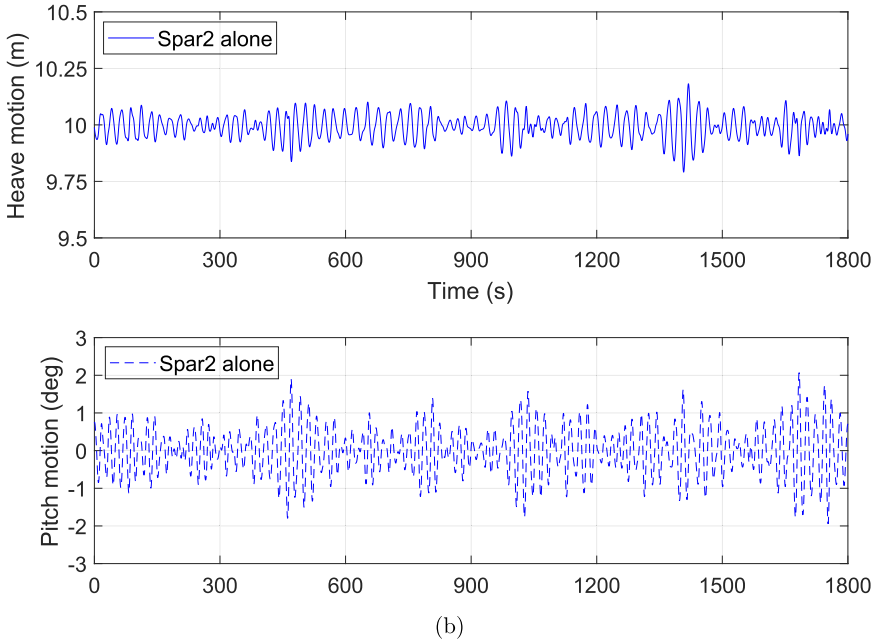

(b)

Fig. 19. Time series of numerical simulation of Spar2, $H_s = 2.0$ m, $T_p = 16$ s, Seed No.1.

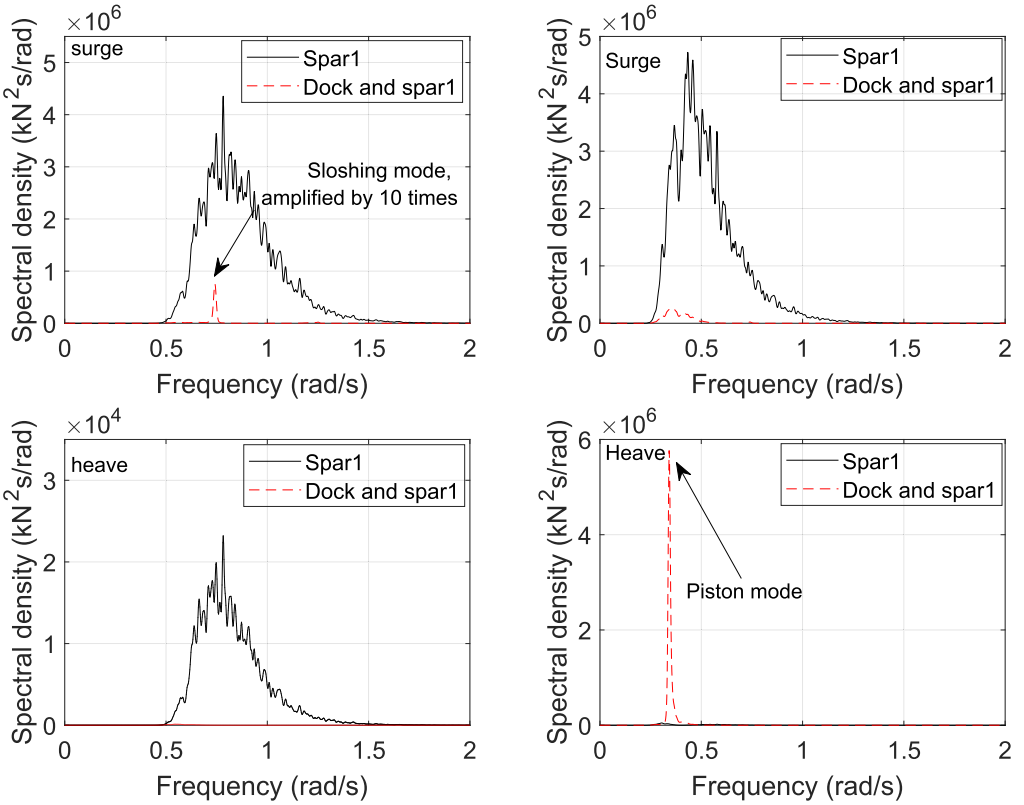

(a) T_p=8 s (b) T_p=16 s

Fig. 20. Spectra of first-order wave forces acting on Spar1, H_s = 2 m

calculation was done using (9)–(11), where η_{MPM} is the estimated MPM, p equals 0.37, σ is the standard deviation of the individual maxima, $\bar{\eta}$ is the mean value of the maxima, and γ is the Euler constant.

$$\eta_{MPM} = -\ln[-\ln(p)]\beta + \mu \tag{9}$$

$$\beta = \frac{\sqrt{6}}{\pi}\sigma \tag{10}$$

$$\mu = \bar{\eta} - \frac{\sqrt{6}}{\pi}\sigma\gamma \tag{11}$$

For mating of a wind turbine tower onto a spar foundation, the relative heave velocity between the tower and spar is governing. If the relative heave velocity exceeds the winch capacity, the mating task will be difficult. For mating of a wind turbine blade, the relative motion in the horizontal plane between the hub and blade is critical [20]. In the following, only statistical results of the heave velocity and pitch motion are analysed. It is assumed that the relative heave velocity between the dock and spar can represent that between the wind turbine tower and spar, and the relative pitch motion can be representative of the planar motion between the blade and hub.

Fig. 24 presents statistics of the absolute and relative response MPMs of the spars for an *Hs* of 2 m. Generally, the MPMs increase with *Tp*. This trend applies to both the heave velocity and the platform-pitch. As the natural periods of the spars and the dock are above 16 s, such a trend is reasonable. Compared against the spar-alone case, the dock reduces the heave velocity of Spar1 when *Tp* is below 10 s. However, when *Tp* exceeds 10 s, the dock has a negative impact because of the piston-mode resonance. The relative heave velocity between Spar1 and the dock becomes especially large when *Tp* approaches 16 s because the resonant response of the dock in heave is dominant. Thus, the present design of the dock faces difficulties when it comes to mating of wind turbine towers in swell. As shown in

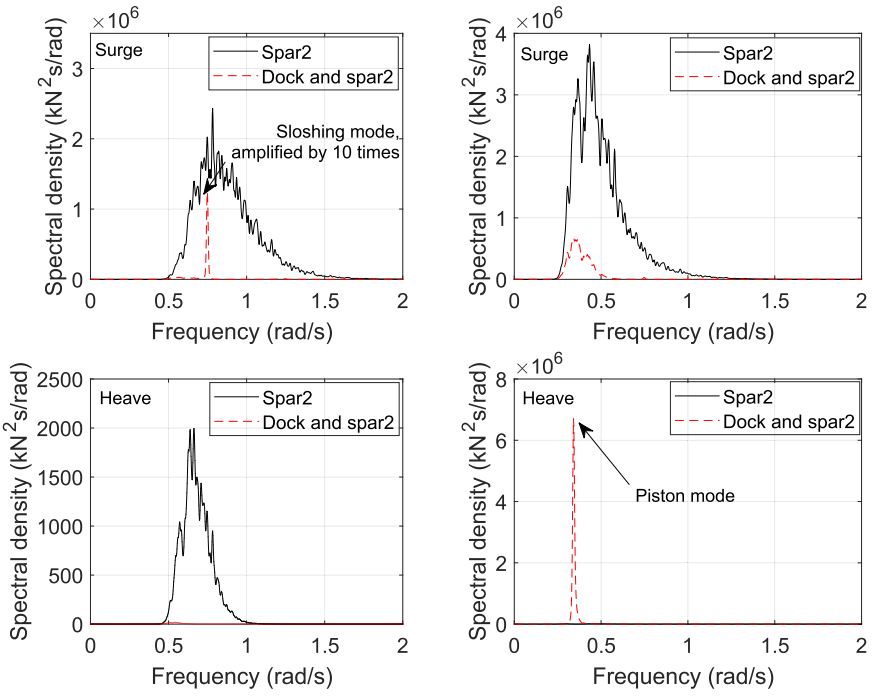

(a) T_p=8 s (b) T_p=16 s

Fig. 21. Spectra of first-order wave forces acting on Spar2, H_s = 2 m

Fig. 24(b), the dock is effective in reducing the platform-pitch of Spar1, although the effect is greater when *Tp* is below 12 s. This observation indicates the potential of the dock in facilitating the blade mating process. For $Hs = 2$ m, if the threshold value of platform-pitch is 1 deg, the dock can extend the weather window from $Tp = 10$ s to $Tp = 12$ s. The MPM values of Spar2 are presented in Fig. 24 (c)–24(d). Compared with Spar1, Spar2 has reduced heave velocity and platform-pitch because of the increased mass inertia and natural periods in heave and pitch. Still, the influence of the dock is analogous.

Here, we focus on the relative motion between the floating dock and spar which is an indicator that affects the actual mating processes. The MPMs under two different *Hs* are compared in Fig. 25. When $Tp \leq 8$ s, the relative heave velocity is limited and on the order of 10^{-3} m/s in both conditions and for both spars, and the relative platform-pitch is amplified by two to four times when *Hs* increases from 1 m to 2 m. When $Tp \geq 10$ s, the heave velocity or the platform-pitch MPMs are governed by first-order motions, and the relative platform-pitch is amplified approximately twice when *Hs* increases from 1 m to 2 m. If thresholds of specific mating operations are known, the operational limits in terms of *Hs* and *Tp* for mating operations can be back derived; see Refs. [34,37] for examples. As acceptance criteria for the mating processes are not the foci of this paper, specific operational limits are not pursued here. Generally, Spar2 has lower MPMs than Spar1 and the operational limits of Spar2 are expected to be higher.

6.5.4. *Free surface elevation inside the dock*

As the present time-domain analysis approach does not produce the free surface elevation inside the dock, we adopt a frequency-domain approach for a simplified analysis here. The relation between the response variable and the incoming wave can be described as follows [33].

$$Y(t) = \zeta_a \cdot Re\left[H_Y(\omega)e^{i\omega t}\right] \tag{12}$$

where *Y* is the free surface elevation inside the dock, ζ_a is the amplitude of the incoming wave, $H_Y(\omega)$ is the complex transfer function, ω is the circular frequency, *t* is the time, and *Re* is the notation for the real part of a complex number.

For long-crested waves, the *i*-th order spectral moment of *Y* can be expressed as

$$m_i = \int_0^\infty \omega^i \left|H_Y(\omega)\right|^2 S(\omega)d\omega \tag{13}$$

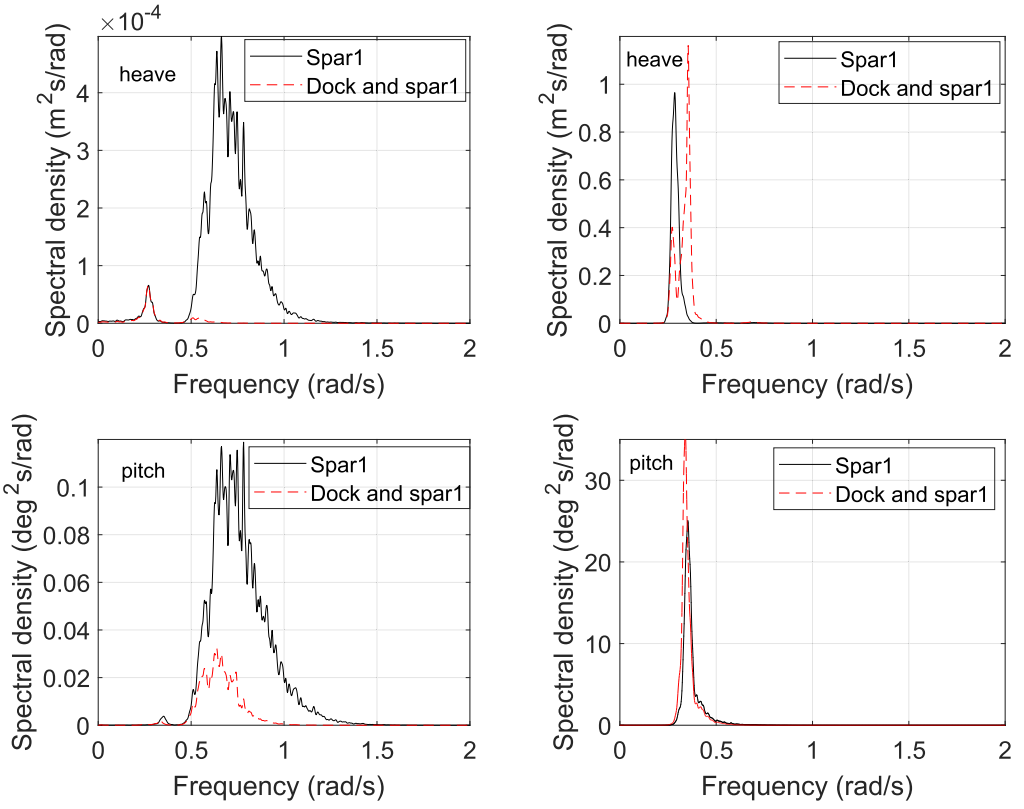

(a) T_p=8 s (b) T_p=16 s

Fig. 22. Spectra of motion responses of Spar1, H_s = 2 m

where $S(\omega)$ is the wave spectrum, e.g., PM or JONSWAP spectrum [35]. Then, the mean zero-upcrossing period Tz is related to the zero-th and second-order moments of the response spectrum and is given by

$$Tz = 2\pi\sqrt{\frac{m_0}{m_2}} \tag{14}$$

Under the narrow band assumption, the number of zero upcrossing equals the number of response maxima and can be determined as follows

$$N_s = \frac{Tref}{Tz} \tag{15}$$

where *Tref* is the duration of the short-term seastate. So, the most probable largest wave elevation can be found as

$$Y_{MPM} = \sqrt{2m_0 \cdot lnN_s} \tag{16}$$

where *ln* is the natural logarithm.

As a spar is assumed to be positioned at the coordinate origin (Fig. 13) during installation, the RAO of the free surface elevation for Point 1 (Fig. 10) is relevant. After applying (12)–(16), we estimated the MPM values for the single-peaked PM spectrum with $Hs = 1$ m. A reference period of 1800 s is considered as before. In Table 8, the subscripts u and d refer to the undamped and damped cases, respectively; refer to Sec. 3.2. Y_{MPM} is sensitive to Tp and to the damping option. When Tp is below 12 s, Y_{MPM}, u is very small for the undamped case, whereas Y_{MPM}, d varies between 0.1 and 0.3 m for the damped case. These small Y_{MPM}, u values arise because the high-

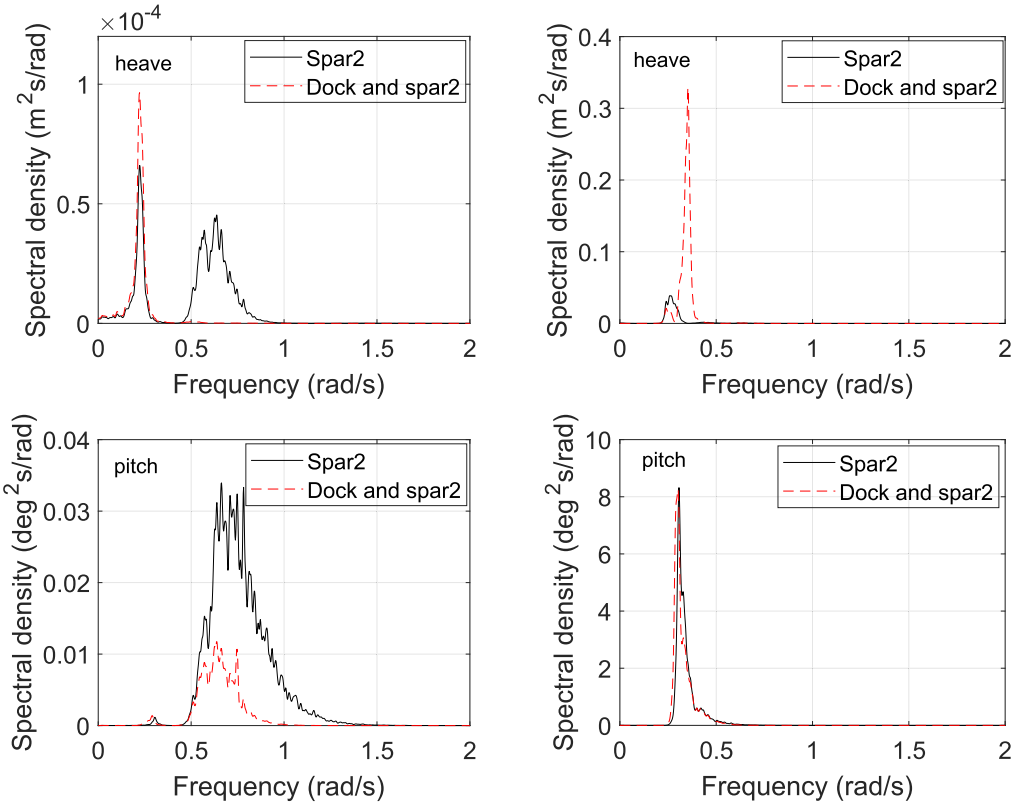

(a) T_p=8 s (b) T_p=16 s

Fig. 23. Spectra of motion responses of Spar2, H_s = 2 m

order resonances of the moonpool are not captured by the RAO. When $Tp \geq 14$ s, there is an appreciable increase in Y_{MPM} due to an influence of the piston-mode resonance. Y_{MPM}, u exceeds 1 m and Y_{MPM}, d is approximately 40% lower. Although the present simplified analysis applies to the single floating dock, the trend of variation of Y_{MPM} with regard to Tp agrees with that of the heave and pitch responses of the spars in the coupled time-domain analysis. If the damping level increases, Y_{MPM} is expected to reduce further.

7. Conclusions

We develop the concept of a large floating dock for installation of spar floating wind turbines. The basic geometry and functionality of the dock is introduced, and the outcome of a design optimisation is presented considering 11 design variables with nonlinear design constraints. Based on the optimum dock design, hydrodynamic analysis of the dock with a spar inside was performed, and a mooring system was designed. Finally, dynamic response analysis of the optimum dock with two different spar foundations was conducted under irregular wave conditions. The main conclusions are as follows:

1. During the dock design, complex design constraints should be considered. The draft limitation of the dock in transit and the hydrostatic stability criteria in transit play an important role in the optimisation.
2. Hydrodynamic analysis using the linear potential-flow method reveals the highest sloshing mode and the piston-mode resonance of the dock. It is difficult to avoid the sloshing phenomenon unless the dock is designed with a very large inner diameter.
3. From the coupled dynamic response analysis in the time domain, one can observe the hydrodynamic excitation forces due to sloshing and piston-mode resonance. The motion responses of the spar inside the dock is sensitive to the wave spectral peak periods. The piston-mode resonance induces significant spar motions when the wave period exceeds 14 s.

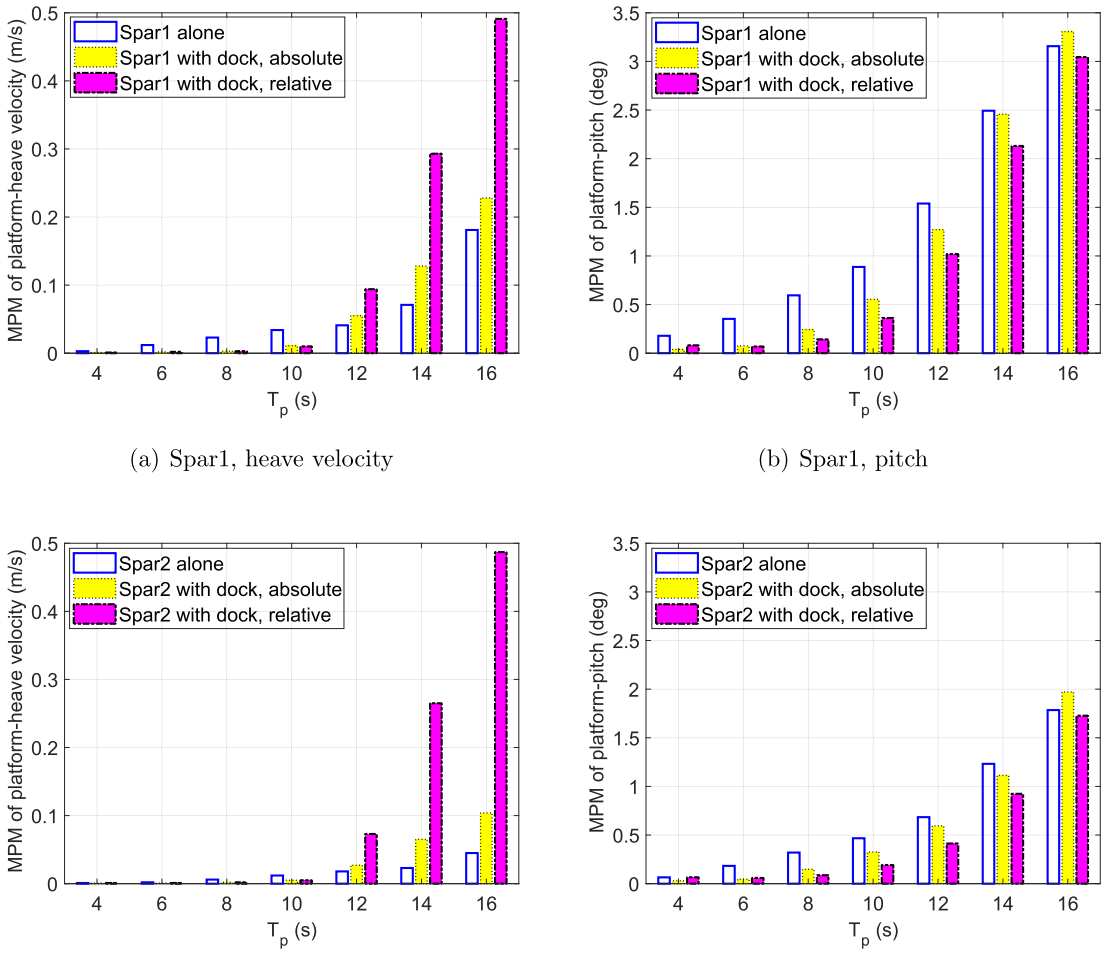

(a) Spar1, heave velocity

(b) Spar1, pitch

(c) Spar2, heave velocity

(d) Spar2, pitch

Fig. 24. Response statistics of motion responses of Spar1 and Spar2, $H_s = 2$ m; most probable maximum (MPM) obtained based on Gumbel fit of 20 seeds.

4. Among the two spar foundations considered, Spar1 has a draft of 96.3 m and Spar2 has a draft of 133.6 m with greater weight. Motion response spectra and response statistics show that the dock reduces the heave velocity of both spars when $Tp \leq 10$ s, and reduces the platform-pitch motions under all Tp investigated. Thus, the dock is expected to increase the operational limits for blade mating. However, with the dock and near $Tp = 16$ s, the heave velocity of the spars are deteriorated due to the piston-mode resonance and the pitch motion responses are still large primarily due to the sloshing effects. Thus, using the dock for tower mating under swell conditions is difficult. Spar2 is heavier than Spar1 and has higher natural periods in heave and pitch, and the dynamic responses of Spar2 are less. Generally, the dock influences the two spars in a similar way.
5. From the frequency-domain analysis, the response amplitude operators of Spar1 and Spar2 with and without the dock are obtained. The influence of the dock on the heave and pitch motions of the spars is visible. Although the frequency-domain analysis only considers the hydrodynamic couplings and ignores the mechanical couplings, the observation of the dock's effect on the spar motions agrees with that of the time-domain simulation.
6. The free surface elevation inside the dock is estimated from a simplified frequency-domain approach. With a small damping level applied, the most probable surface elevation reaches 1 m when Tp approaches the piston-mode resonance period. The trend of variation in the free surface elevation is similar to that of the heave and pitch responses of the spars in the coupled time-domain analysis.

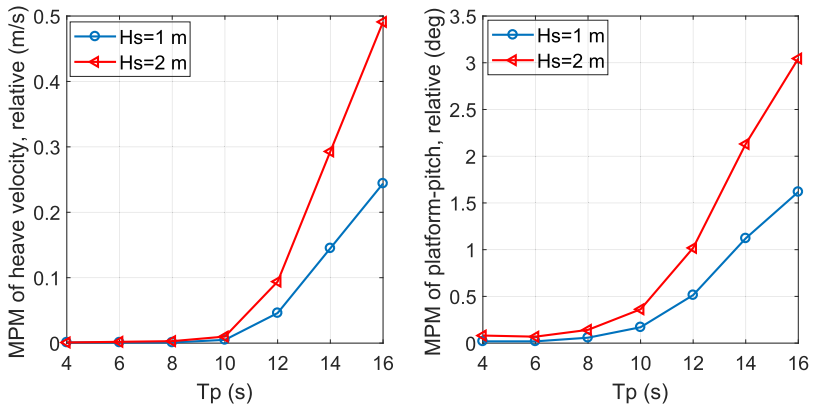

(a) Spar1

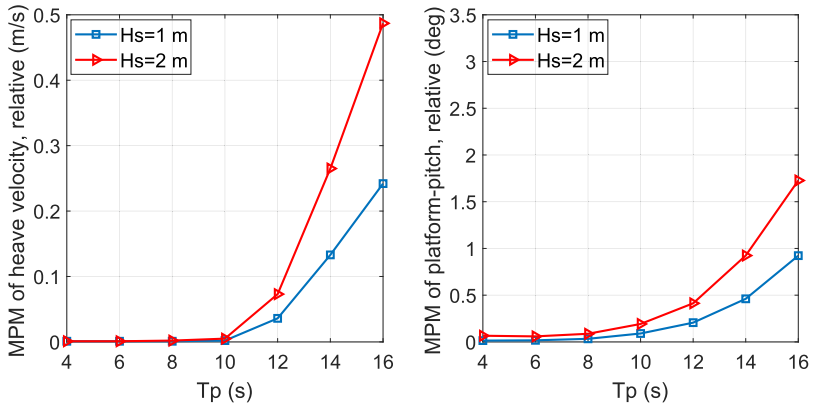

(b) Spar2

Fig. 25. Comparison of MPMs of relative motions between the spars and the dock in $H_s = 1$ m and $H_s = 2$ m

Table 8
Estimate of free surface elevation at Point 1 of Fig. 9(a) (*Hs*=1 m, *Tref* = 1800 s).

Tp (s)	Tz, u (s)	Y_{MPM}, u (m)	Tz, d (s)	Y_{MPM}, d (m)
4	4.15	0.0116	4.54	0.1514
6	4.70	0.0125	5.36	0.2862
8	5.30	0.0097	5.61	0.2290
10	13.90	0.0365	6.06	0.1177
12	17.40	0.3575	10.08	0.2400
14	17.87	1.0312	16.54	0.5661
16	18.40	1.6947	18.66	1.0140

8. Limitations and future work

The scope of this work is limited. In the hydrodynamic analysis, only a potential-flow code was applied, and complex hydrodynamics including nonlinear sloshing cannot be captured by the present numerical model. The dynamic analysis focuses on the stage when the spar foundation has already been placed inside the dock and wind turbine components are to be installed. Stages like towing or ballasting of the dock are not addressed. Experimental investigation of the concept and advanced hydrodynamic analysis is currently under way. As the piston-mode resonance is identified as a phenomenon that jeopardises the motion performance of the spar, measures may be taken. A dock with alternative shapes can be considered in order to achieve higher piston-mode period. To avoid the sloshing problem, the door of the dock may be left open during operation. In the design optimisation, 11 design variables were addressed. In future, additional design variables may be considered, and a detailed design of the internal structure should be carried out. The structural design should address the stress concentration and fatigue life of the gate opening and internal compartments.

Acknowledgements

This work has been partially supported by the Research Council of Norway granted through the Centre for Research-based Innovation of Marine Operations (SFI MOVE) at Norwegian University of Science and Technology (NTNU) (RCN project 237929). The authors acknowledge discussions with Karl Henning Halse, Trygve Kristiansen and Mael Korentin Ivan Moreau of NTNU, Giovanni Battista Picotti and Øystein Johannessen of Equinor ASA, Petter Andreas Berthelsen of SINTEF Ocean AS, and Lin Li of University of Stavanger.

References

[1] Sclavounos P, Lee S, DiPietro J, Potenza G, Caramuscio P, De Michele G. Floating offshore wind turbines: tension leg platform and taught leg buoy concepts supporting 3-5 MW wind turbines. In: European wind energy conference EWEC; 2010. p. 20–3.
[2] Pineda I, Tardieu P. The European offshore wind industry key trends and statistics. https://windeurope.org/about-wind/statistics/offshore/european-offshore-wind-industry-key-trends-and-statistics-2016/. [Accessed 1 June 2017].
[3] Steen KE. Hywind Scotland – status and plans. http://www.sintef.no/projectweb/deepwind_2016/presentations/. [Accessed 1 February 2017].
[4] Jonkman JM, Buhl Jr ML. FAST user's guide-updated august 2005. Technical Report. Golden, CO., USA: National Renewable Energy Laboratory; 2005.
[5] Larsen TJ, Hansen AM. How 2 HAWC2, the user's manual, technical report. Denmark: Risø National Laboratory; 2007.
[6] Moné C, Stehly T, Maples B, Settle E. 2015 cost of wind energy review. Technical Report, NREL/TP-6A20-66861. Denver, CO, USA: NREL; 2015.
[7] Sarkar A, Gudmestad OT. Study on a new method for installing a monopile and a fully integrated offshore wind turbine structure. Mar Struct 2013;33:160–87.
[8] Acero WG, Gao Z, Moan T. Numerical study of a novel procedure for installing the tower and rotor nacelle assembly of offshore wind turbines based on the inverted pendulum principle. J Mar Sci Appl 2017;16:243–60.
[9] Esteban M, Couñago B, López-Gutiérrez J, Negro V, Vellisco F. Gravity based support structures for offshore wind turbine generators: review of the installation process. Ocean Eng 2015;110:281–91.
[10] Ren Z, Jiang Z, Gao Z, Skjetne R. Active tugger line force control for single blade installation. Wind Energy 2018;21:1344–58.
[11] Verma AS, Jiang Z, Vedvik NP, Gao Z, Ren Z. Impact assessment of a wind turbine blade root during an offshore mating process. Eng Struct 2019;180:205–22.
[12] Myhr A, Bjerkseter C, Ågotnes A, Nygaard TA. Levelised cost of energy for offshore floating wind turbines in a life cycle perspective. Renew Energy 2014;66:714–28.
[13] lIEN KH. Hywind Scotland – marine operations. http://www.norcowe.no/doc/konferanser/2016/. [Accessed 1 February 2017].
[14] Smith I, Lewis T, Miller B, Lai P, Frieze P. Limiting motions for jack-ups moving onto location. Mar Struct 1996;9:25–51.
[15] Equinor ASA. Hywind installation. https://www.equinor.com/en/how-and-why/innovate/the-hywind-challenge.html. [Accessed 1 February 2018].
[16] Hatledal LI, Zhang H, Halse KH, Hildre HP. Numerical simulation of novel gripper mechanism between catamaran and turbine foundation for offshore wind turbine installation. In: ASME 2017 36th international conference on ocean, offshore and arctic engineering. American Society of Mechanical Engineers; 2017. OMAE2017–62342.
[17] Jiang Z, Li L, Gao Z, Halse KH, Sandvik PC. Dynamic response analysis of a catamaran installation vessel during the positioning of a wind turbine assembly onto a spar foundation. Mar Struct 2018;61:1–24.
[18] Jiang Z, Ren Z, Gao Z, Sandvik PC, Halse KH, Skjetne R. Mating control of a wind turbine tower-nacelle-rotor assembly for a catamaran installation vessel. In: The 28th international ocean and polar engineering conference. International Society of Offshore and Polar Engineers; 2018.
[19] Wang W, Bai Y. Investigation on installation of offshore wind turbines. J Mar Sci Appl 2010;9:175–80.
[20] Jiang Z, Gao Z, Ren Z, Li Y, Duan L. A parametric study on the final blade installation process for monopile wind turbines under rough environmental conditions. Eng Struct 2018;172:1042–56.
[21] Faltinsen O, Timokha A. Sloshing. Cambridge University Press; 2009.
[22] DNV GL. Offshore standard DNV-OS-C101-design of offshore steel structures. General - LRFD method; 2016.
[23] International Maritime Organization. Code for the construction and equipment of mobile offshore drilling units. 2009.
[24] DNV GL. Offshore standard DNVGL-OS-C301, stability and watertight integrity. 2017.
[25] DNV GL. Offshore standard DNV-OS-H101. Marine Operations; 2011. General.
[26] Gaunaa M, Bergami L, Guntur S, Zahle F. First-order aerodynamic and aeroelastic behavior of a single-blade installation setup. In: Journal of physics: conference series, vol. 524. IOP Publishing; 2014, 012073.
[27] DNV GL. SESAM user manual WADAM wave analysis by diffraction and Morison theory. 2019. valid from program version 9.6.
[28] MathWorks Inc. Optimization toolbox for use with MATLAB R2016b: user's guide. 2016., Version 7.5.
[29] Newman J. Progress in wave load computations on offshore structures. In: Proceedings of the 23rd international conference offshore mechanics & arctic engineering, vancouver, Canada; June, 2004. p. 20–5.
[30] DNV GL. SESAM Tutorial HydroD - creation and use of surface meshes. 2017.
[31] MARINTEK. MIMOSA User's documentation. 2012., Version 6.3-06.
[32] MARINTEK. SIMO Theory Manual. 2016., Version 4.8.4.
[33] Faltinsen O. Sea loads on ships and offshore structures, vol. 1. Cambridge university press; 1993.
[34] Jiang Z, Acero WG, Gao Z, Li L. A numerical study on a flopper stopper for leg positioning of a jack-up barge. In: ASME 2017 36th international conference on ocean, offshore and arctic engineering. American Society of Mechanical Engineers; 2017. V009T12A028–V009T12A028.
[35] DNV GL. Recommended practice DNV-RP-C205, environmental conditions and environmental loads. 2010.
[36] DNV GL. Offshore standard DNV-OS-E301 position mooring. 2008.
[37] Guachamin-Acero W, Jiang Z, Li L. Numerical study of a concept for major repair and replacement of offshore wind turbine blades. Wind Energy; 2020. p. 1–19. https://doi.org/10.1002/we.2509.